BremHLR

Kompetenzzentrum für Höchstleistungsrechnen Bremen

Statusbericht 2012

des

Kompetenzzentrums

für

Höchstleistungsrechnen Bremen

– BremHLR –

Bremen, Juli 2013

Universität Bremen

JACOBS UNIVERSITY

ALFRED-WEGENER-INSTITUT
HELMHOLTZ-ZENTRUM FÜR POLAR- UND MEERESFORSCHUNG

Hochschule Bremerhaven

HLRN

Norddeutscher Verbund für Hoch- und Höchstleistungsrechnen

www.bremhlr.uni-bremen.de

Das Berichtsjahr 2012 in Stichpunkten

- Weitere Steigerung der Bremer Nutzung der Computer des Norddeutschen Verbunds für Hoch- und Höchstleistungsrechnen (HLRN)
- 7. Workshop zur Einführung in die parallele Programmierung
- Mitarbeit des BremHLR am Ausschreibungsverfahren für das Nachfolgesystem HLRN-III am HLRN
- Ausblick auf das zukünftige Rechnersystem HLRN-III

Inhaltsverzeichnis

1 Das BremHLR: Aufgaben und organisatorische Struktur

1.1 Aufgaben

Das Land Bremen beteiligt sich am Norddeutschen Verbund für Hoch- und Höchstleistungsrechnen – HLRN – um an dem rasanten Fortschritt der Computer- und Softwaretechnologie Teil zu haben. Das Kompetenzzentrum für Höchstleistungsrechnen Bremen – BremHLR – unterstützt dazu Wissenschaftler im wissenschaftlichen Rechnen insbesondere im Land Bremen. Unterstützung wird für Projekte sowohl in der Konzeption, der Antragstellung als auch der Durchführung geleistet. Der Schwerpunkt der Unterstützung liegt hierbei auf Projekten auf dem HLRN-System. Seit 2005 wurde die Betreuung aber auch auf Rechenprojekte an den nationalen Höchstleistungsrechenzentren wie z. B. dem John von Neumann-Institut für Computing (NIC) in Jülich ausgeweitet.

Als Bestandteil im Kompetenznetzwerk des HLRN beteiligt sich BremHLR unter anderem an der fachspezifischen Nutzerberatung, der Pflege von Software-Paketen und der Veranstaltung überregionaler Nutzerworkshops. Die Geschäftsstelle des BremHLR ist an der Universität Bremen im Zentrum für Technomathematik angesiedelt.

Das BremHLR wurde am 1. Juli 2003 als Kooperation zwischen der Universität Bremen (UB), der Jacobs University Bremen (JUB) und dem Alfred-Wegener-Institut für Polar- und Meeresforschung (AWI) gegründet. Seit April 2008 ist auch die Hochschule Bremerhaven (HBHV) Kooperationspartner des BremHLR. Das Kompetenzzentrum wird von den beteiligten Kooperationspartnern sowie der Bremer Senatorin für Bildung und Wissenschaft (SfBW) finanziell getragen.

1.2 Struktur

Dem Lenkungsausschuss des BremHLR als oberstes beschlussfassendes und steuerndes Gremium gehören Vertreter der kooperierenden Einrichtungen an. Im Einzelnen sind dies:

- Prof. Dr. Alfred Schmidt (UB/Zentrum für Technomathematik ZeTeM)
- Prof. Dr. Wolfgang Hiller (AWI/Rechenzentrum)
- Prof. Dr. Ulrich Kleinekathöfer (JUB)
- Prof. Dr. Stephan Frickenhaus (HBHV)
- Helmuth Wolf (SfBW)

Die fachspezifische Betreuung der Projekte am Norddeutschen Verbund für Hoch- und Höchstleistungsrechnen (HLRN) sowie von Projekten an anderen nationalen Höchstleistungsrechenzentren wird von den Fachberatern des BremHLR geleistet, die ebenfalls den Einrichtungen der Kooperationspartner angehören. Im Berichtszeitraum waren folgende Fachberater tätig:

- Dr. Lars Nerger (AWI/Rechenzentrum, UB/ZeTeM, Leiter Geschäftsstelle)
- Thorsten Coordes (UB/ZARM)
- Dr. Achim Geleßus (JUB/CLAMV)
- Dr. Natalja Rakowsky (AWI/Rechenzentrum)

Die Geschäftsstelle ist verantwortlich für die Organisation der Workshops (siehe Abschnitt Veranstaltungen) und die Unterstützung der Nutzer, insbesondere im Antragsverfahren. Das Sekretariat der Geschäftsstelle wird betreut von

- Julitta von Deetzen.

2 Tätigkeitsprofil des BremHLR im Berichtszeitraum

2.1 Unterstützung der HLRN-Nutzung im Land Bremen

Ein Schwerpunkt der Aktivitäten des BremHLR lag auch in diesem Berichtszeitraum in der Unterstützung der HLRN-Nutzung. Neben den Tätigkeiten von Wolfgang Hiller als Mitglied der Technischen Kommission sowie Alfred Schmidt als Mitglied des Wissenschaftlichen Ausschusses bestand die Unterstützung des HLRN durch das BremHLR hauptsächlich in der Fachberatung für Bremer Projekte am HLRN von der Antragstellung bis zur Begleitung rechenintensiver Projekte während der gesamten Projektlaufzeit.

Als besondere Aufgabe waren Mitglieder des Lenkungsausschusses und der Fachberater am Ausschreibungsverfahren für das nächste HLRN Höchstleistungsrechnersystem (HLRN-III) beteiligt. Die BremHLR-Mitglieder beteiligten sich hierbei an der Formulierung des Leistungsverzeichnisses sowie an der Auswertung und Bewertung der Benchmarkergebnisse die von den Anbietern eingereicht wurden.

2.2 Weitere Aktivitäten des BremHLR

Im Veranstaltungsjahr 2012 wurde vom BremHLR der *7. Workshop zur Einführung in die parallele Programmierung mit MPI und OpenMP* organisiert und durchgeführt. Mit 24 Teilnehmern war dieser Workshop wieder sehr gut besucht.

Der Workshop wurde in der Zeit vom 9. bis zum 13. Januar an der JUB abgehalten. Als Referenten konnte wie bereits bei bisherigen Workshops Dr.-Ing. Wolfgang Baumann und Dr. Hinnerk Stüben vom Konrad-Zuse-Zentrum für Informationstechnik Berlin gewonnen werden. Für die Studenten der JUB wurde der Workshop auch wieder als offizielle Lehrveranstaltung angeboten. Durch die Bearbeitung einer abschließend bewerteten Übungsaufgabe konnten die Studenten Kreditpunkte für ihr Bachelor- und Masterstudium erlangen.

Der sehr gute Zuspruch und der große Erfolg der Veranstaltungen zeigt deutlich den dringenden Bedarf zur Ausbildung im Hoch- und Höchstleistungsrechnen und gibt Anlass dazu, solche Workshops auch weiterhin als regelmäßige Ausbildungs- und Schulungsmaßnahme anzubieten.

Auch im aktuellen Berichtszeitraum war das BremHLR weiteren Veranstaltungen beteiligt. Fachberater des BremHLR beteiligten sich unter anderem an einem Fachberaterworkshop an denen unterschiedliche Themen des HLRN-Betriebs und der Nutzerbetreuung besprochen wurden. Eine Übersicht über die Veranstaltungen ist in Abschnitt 4 zu finden.

3 Statistische Angaben zu den Bremer Höchstleistungsprojekten

Im Jahr 2011 setzte sich der Trend der intensiven Nutzung des HLRN durch die Bremer Projekte bei gleichzeitig steigendem Bedarf an Rechenleistung fort. Für Bremer Projekte wurde für das Jahr 2012 fast doppelt so viel Rechenzeit bewilligt wie für das Jahr 2011. Im Jahresdurchschnitt wurde ein prozentualer Anteil von 7,7 % an der gesamten am HLRN verfügbaren Rechenleistung erreicht. Dieses liegt deutlich über dem investiven Anteil des Landes Bremen am HLRN. Der gesteigerte Bedarf ist darauf zurückzuführen, dass sich der Bedarf an Rechenleistung, z.B. durch höher aufgelöste Modellgitter, in den einzelnen Projekten vergrößert hat.

Insgesamt wurden im Jahr 2012 etwa 924 000 NPL[1] durch Bremer Projekte am HLRN abgenommen. Gegenüber dem Vorjahr ist der Verbrach damit um etwa 45% gestiegen und entspricht in etwa 14 Millionen CPU-Stunden. Abbildung 3.1 zeigt den monatlichen Verbrauch der Bremer Projekte am HLRN. Im Jahr 2012 hat sich die Bremer Nutzung auf hohem Niveau stabilisiert.

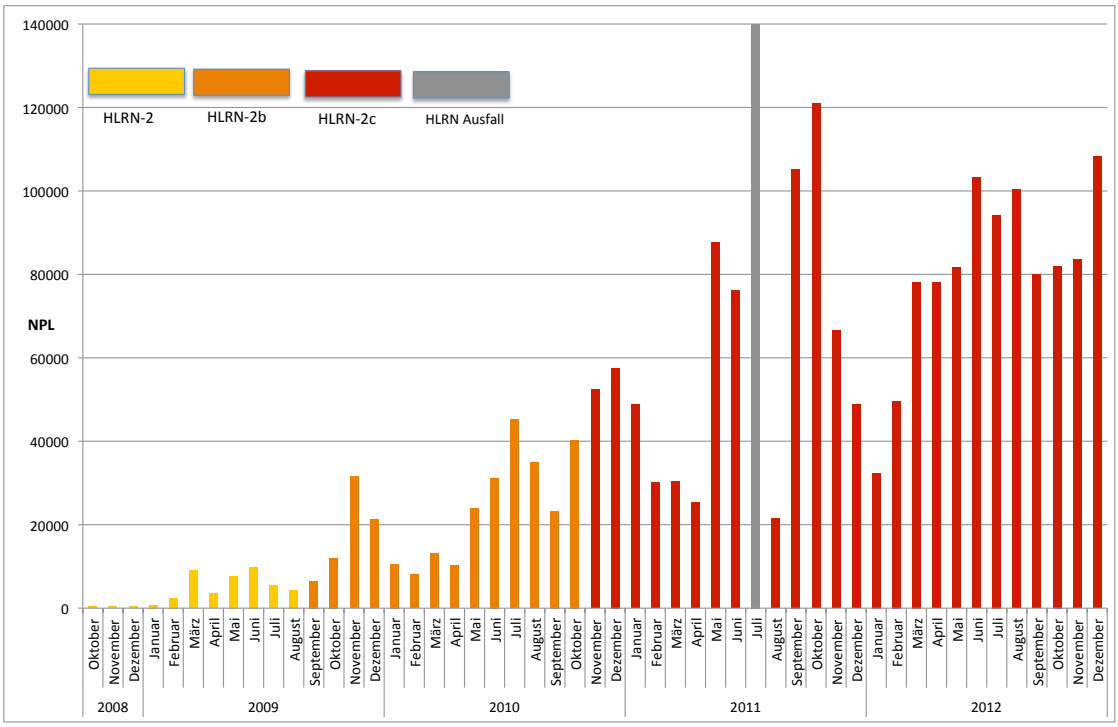

Abbildung 3.1: Grafische Darstellung des monatlichen Rechenzeitverbrauchs der Bremer HLRN-Großprojekte. Verbrauch in der HLRN-Leistungseinheit NPL zwischen Oktober 2008 und Dezember 2012. Die Farben zeigen die Verfügbarkeit der unterschiedlichen Ausbaustufen der HLRN-Systeme. Im Juli 2011 waren die HLRN-Systeme nicht nutzbar, da der Zugang zu den Computern wegen eines Rechnereinbruchs vorrübergehend geschlossen werden musste. Auch im August 2011 konnten die HLRN-Systeme nur teilweise genutzt werden.

[1] Norddeutsche Parallelrechner-Leistungseinheit: Auf den Systemen der ersten Ausbaustufe entspricht 1 NPL einer CPU-h auf drei Knoten mit je 8 Prozessorkernen. Auf den Systemen der zweiten Ausbaustufe entspricht 1 NPL einer CPU-h auf 12 Prozessorkernen und auf der dritten Stufe entspricht 1 NPL einer CPU-h auf 16 Prozessorkernen.

Eine Übersicht zu allen vom BremHLR betreuten Projekten gibt Tabelle 3.1. Im Jahr 2012 wurden vom BremHLR 21 Projekte am HLRN betreut. Die Anzahl der am HLRN akkreditierten Nutzer, die die Projekte durchführen, ist leicht von 69 auf 79 angestiegen. Es wurden im Jahr 2012 mehrere Neuanträge für Projekte mit großem Rechenzeitbedarf gestellt und vom Wissenschaftlichen Ausschuss des HLRN bewilligt.

Tabelle 3.1: Übersicht der Bremer HPC-Projekte, die innerhalb des Berichtszeitraums vom BremHLR betreut wurden. Status: F = Fortsetzung, E = Erstantrag; NPL: Kontingent in NPL im Jahr 2012

Kennung	Projektleiter	Institut	Laufzeit	NPL	Status
hbc00001	Dr. P. Deák/Dr. B. Aradi	UB/BCCMS	I/09 – I/12	16000	F
hbc00010	Prof. T. Frauenheim	UB/BCCMS	II/11 – I/12	24000	E
hbc00011	Dr. P. Deák/Dr. B. Aradi	UB/BCCMS	II/12 – II/13	105000	E
hbc00012	Prof. L. Colombi-Ciacchi	UB/BCCMS	IV/12 – III/13	5000	E
hbc00013	Dr. J. Larrucea	UB/BCCMS	IV/12 – III/13	30000	E
hbi00011	Dr. M. Walter	UB & JUB	I/11 – II/12	12000	E
hbi00014	Dr.-Ing. R. Groll	UB/ZARM	I/11 – III/13	45000	F
hbi00015	Dr.-Ing. R. Groll	UB/ZARM	III/11 – III/13	60000	F
hbk00018	Dr. K. Weigel	UB/IUP	I/11 – IV/13	21000	F
hbk00021	Prof. Dr. T. Jung	AWI & UB	II/09 – II/13	274000	F
hbk00025	Prof. Dr. M. Schulz	UB/MARUM	II/10 – II/13	80000	F
hbk00026	Prof. Dr. W. Hiller	AWI & UB	III/10 – II/12	18000	F
hbk00027	Prof. Dr. M. Schulz	UB/MARUM	III/10 – IV/12	68000	F
hbk00028	Prof. Dr. P. Lemke	AWI & UB	IV/11 – III/13	155000	F
hbk00029	Prof. Dr. T. Jung	AWI & UB	II/11 – I/12	25000	E
hbk00030	Prof. Dr. T. Jung	AWI & UB	IV/11 – III/13	149000	F
hbm0001	Prof. T. Frauenheim	UB/BCCMS	III/12 – II/13	28000	E
hbp00003	Prof. Dr. C. Lämmerzahl/ Prof. Dr. S. Rosswog	UB & JUB	IV/10 – III/13	173000	F
hbp00010	Prof. Dr. C. Lämmerzahl/ Prof. Dr. M. Brüggen	UB & JUB	I/11 – II/12	2000	E
hbp00011	Prof. T. Frauenheim	UB/BCCMS	IV/11 – III/13	44000	F
hbp00015	Prof. T. Frauenheim	UB/BCCMS	II/12 – II/13	30000	E

4 Veranstaltungen mit Beteiligung des BremHLR

7. BremHLR-Workshop *Einführung in die Programmierung mit MPI und OpenMP*

Veranstalter: BremHLR

Datum: 9. – 13. Januar 2012

Ort: Jacobs University Bremen

Beschreibung: In dem Workshop wurden die Grundlagen der parallelen Programmierung vermittelt. Der Schwerpunkt lag auf den Programmiermodellen MPI und OpenMP. Praktische Übungen bildeten einen wesentlichen Teil des Workshops.

Referenten: Dr.-Ing. Wolfgang Baumman und Dr. Hinnerk Stüben (Konrad-Zuse-Zentrum für Informationstechnik Berlin, ZIB)

Teilnehmerzahl: 24

Teilnehmende Institutionen: AWI, BSH, JUB, UB (IUP, ITP, Mathematik, Physik)

22. HLRN-Fachberater-Workshop

Veranstalter: HLRN, RRZN Hannover

Datum: 14. – 15. Mai 2012

Ort: Universität Rostock

Teilnehmerzahl: 14

Teilnehmende Institutionen: BremHLR (ZARM), BTU Cottbus, FU Berlin, IOW, IT- und Medienzentrum Uni Rostock, RZ TU Hamburg-Harburg, CMS Humboldt-Uni Berlin, RZ Uni Kiel, Uni Potsdam, ZIB

5 Informationen zur Infrastruktur: Ausblick auf den HLRN-III

Im Laufe des Jahres 2012 wurde aus Ausschreibungsverfahren für das nächste HLRN-System (HLRN-III) durchgeführt. Den Zuschlag bei der Ausschreibung hat die Firma Cray erhalten. Am 17. Dezember 2012 wurden in Hannover und Berlin die Verträge unterzeichnet.

Die Veträge sehen vor, dass das Rechnersystem HLRN-III in zwei Stufen in den Jahren 2013 und 2014 installiert wird. Die erste Installation ist fuer Herbst 2013 vorgesehen. Installiert werden in Hannover und Berlin Supercomputer vom Typ Cray XC30. Das Gesamtsystem in der ersten Ausbaustufe (Herbst 2013) beinhaltet eine massiv parallele (MPP) Komponente bestehend aus

- 1488 Dual-Socket MPP-Knoten, jeweils mit Intel "Next Generation" Xeon E5-Prozessoren
- 93 TB Hauptspeicher verteilt über die Knoten
- Cray Aries Interconnect mit Dragonfly Topologie
- 2.8 PB paralleles Lustre-Dateisystem (“WORK” zur Speicherung von Simulationsdaten) über FDR Infiniband-Netzwerk
- 1 PB Heimat-Dateisystem angebunden an die Knoten per NFS über 10GE-Netzwerk.

Die massiv parallele Komponente wird ergänzt um

- ein SMP-System bestehend aus
  - 32 Dual-Socket-Knoten mit Intel "Next Generation" Xeon-Prozessoren
  - jeweils 256 GB Arbeitsspeicher
  - Dual FDR Infiniband Netzwerk
- 4 Spezialknoten für Pre-/Postprocessing
- Diverse weitere Spezialknoten

Im Herbst 2014 is der Aufbau der zweiten Ausbaustufe geplant. Im Endausbau wird sich das HLRN-III System dann wie folgt darstellen:

- 3552 Dual-Socket MPP-Knoten, jeweils mit Intel "Next Generation" Xeon Prozessoren
- 222 TB Hauptspeicher verteilt über die Knoten
- Cray Aries Interconnect mit Dragonfly Topologie
- 7.2 PB paralleles Lustre-Dateisystem ((“WORK” zur Speicherung von Simulationsdaten) über FDR Infiniband-Netzwerk
- 1 PB Heimat-Dateisystem angebunden an die Knoten per NFS über 10GE-Netzwerk

Die massiv parallele Komponente wird ergänzt um

- ein SMP-System bestehend aus
  - 64 Dual-Socket-Knoten mit Intel "Next Generation" Xeon-Prozessoren
  - jeweils 256 bzw. 512 GB Arbeitsspeicher
  - Dual FDR Infiniband Netzwerk
- 8 Spezialknoten für Pre-/Postprocessing
- Diverse weitere Spezialknoten

6 Projektberichte[2]

6.1 hbc00001: Defect engineering in TiO_2 — from bulk to nanostructures.

HLRN-Projektkennung:	hbc00001
Laufzeit:	I/2009 – I/2012
Projektleiter:	Dr. Peter Deák / Dr. Bálint Aradi
Projektbearbeiter.	Dr. Peter Deák Dr. Bálint Aradi
Institut / Einrichtung:	Bremen Center for Computational Material Science, University of Bremen

TiO_2 is a wide band gap crystalline oxide with many existing and potential applications in environment- and energy-related applications, from photo-catalytic air- and water-purifications to solar and fuel cells. In addition, it is being considered as a transparent conductor for optoelectronics, phase-changing material for resistive memories, and as a room-temperature ferromagnetic semiconductor for spintronics. In most of these applications the understanding of free carrier generation and recombination is of crucial importance. Our research was aimed to establish the fundamental role of intrinsic defects, impurities and dopants in these processes by means of high-level quantum mechanical computations; first in the bulk crystal, and then to apply the gained knowledge for surfaces, interfaces and nanostructures of TiO_2. The task we have set was made difficult by the fact that the “standard tool” of defect calculations – (semi)local exchange-correlation functionals in density functional theory (DFT) – fails for defects in most wide band gap metal oxides. Therefore, we have chosen to test and work with the screened hybrid functional HSE06. In the test phase, we have investigated defects in Group-IV semiconductors (diamond, silicon and germanium), because of the availability of highly reliable experimental data on defects. We have shown that the semi-empirical mixing of screened Hartree-Fock (HF) and GGA (generalized gradient approximation) exchange leads – through error compensation – to a total energy, which is a linear function of the fractional occupation number, as the exact functional ought to be. As a consequence, the electron self-interaction error of the GGA is largely corrected for, which makes it also possible to calculate defect properties with high accuracy [1,2]. Application of the HSE06 functional to TiO_2 has shown that this linearity also holds in TiO_2. This has allowed to reproduce the bulk properties of rutile and anatase, and – for the first time – to provide a quantitative explanation, in agreement with experiment, for charge-carrier self-trapping effects which are different in the two modifications [3,4,5]. Table 1 shows fundamental properties of TiO_2, comparing calculations and experiment. Our HSE06 results improve significantly on earlier (LDA) ones, and are in very good agreement with first-principles many-body methods (GW) and with experiment. Fig. 1a shows the energy density of electronic states, and Fig. 1b the infrared absorption related to the oxygen vacancy in rutile.

[2] Für den Inhalt der Projektberichte sind ausschließlich die genannten Projektleiter bzw. die Projektbearbeiter verantwortlich.

Table 1: Lattice parameters (*a* and *c*), band gap (E_g) and valence band width (VBW) of TiO_2.

anatase	LDA[a]	HSE06	G_0W_0[b]	Exptl.	**rutile**	LDA[a]	HSE06	G_0W_0[b]	Exptl.
a (Å)	3.744	3.755		3.782	*a* (Å)	4.555	4.567		4.587
c (Å)	9.620	9.561		9.502	*c* (Å)	2.922	2.944		2.954
E_g (eV)	2.05	3.58	3.56	[c]	E_g (eV)	1.88	3.37	3.34	3.3 [d]
VBW (eV)	5.0	4.5		4.7 [e]	*VBW* (eV)	6.0	6.4		6.5 [d]

[a] M. Mikami, S. Nakamura, O. Kitao, H. Arakawa, and X. Gonze, Jpn. J. Appl. Phys. **39**, L847 (2000).
[b] W. Kang and M. S. Hybertsen, Phys. Rev. B **82**, 085203 (2010).
[c] The calculations provide the quasiparticle band gap, which can be measured by photoelectron spectroscopy, and is larger than the optical gap, due to excitonic effects and electron-phonon interaction.
[d] Y. Tezuka, S. Shin, T. Ishii, T. Ejima, S. Suzuki, and S. Sato, J. Phys. Soc. Jpn. **63**, 347 (1994).

The quantitative agreement (without any *a posteriori* correction) is striking. The calculations for the vacancy [5] show that all features on the low energy side of the spectrum are related to the neutral vacancy. The positive vacancy (originally thought to be responsible for the main peak) contributes to the broadening on the high energy side. (Because of the handling of charged supercells, the position of the latter absorption peak cannot be calculated accurately, but it should be about 0.6 eV behind the main peak.)

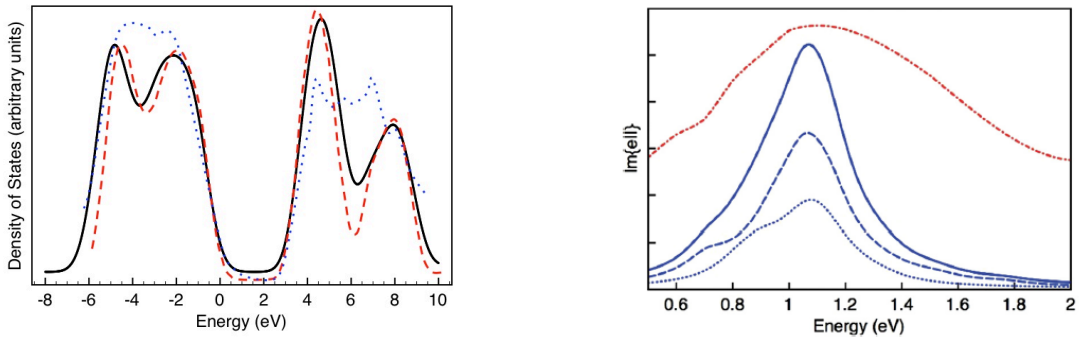

Figure 1: a) Density of states for rutile. Solid line: the present HSE06 calculation, dashed line: the GW calculation of Kwang and Hybersten [Phys. Rev. B **82**, 085203 (2010)], dotted line: experimental PES [Y. Tezuka et al., J. Phys. Soc. Jpn. **63**, 347 (1994)]. b) Infrared absorption of strongly reduced rutile. Solid blue line: sum of the contributions from the nearly degenerate singlet (dotted) and triplet (dashed) states of the neutral oxygen vacancy, dash-dotted line: the experimental IR spectrum of [D. C. Cronemeyer, Phys. Rev. B **113**, 1222 (1059)]. Note: the broadening on the high energy side of the experimental curve is probably due to singly ionized vacancies.

Our calculations have also shown that the neutral oxygen vacancy is only stable in strongly reduced samples, or at very low temperature after illumination with photon energy near the band gap. For vacancy concentrations below 2%, the vacancy auto-ionizes into native electron traps, arising trough the (4+/3+) transitions of Ti atoms in its neighborhood. Fig.2a shows the vertical (adiabatic) charge transition levels relevant to the oxygen vacancy in rutile and in anatase. The rutile results resolve the long existing controversy between observed IR transitions in strongly reduced, and the electron spectroscopy (TL, TSC) and paramagnetic

spectroscopy (EPR) results in more oxidized samples. In the latter, the oxygen vacancy can only hold its two electrons (giving rise to a triplet EPR signal and to the transitions in Fig.1b) if the temperature is very low. Otherwise the electrons will localize on one of the Ti atoms in a wider neighborhood of the doubly positive vacancy, which can only be repopulated by illumination.

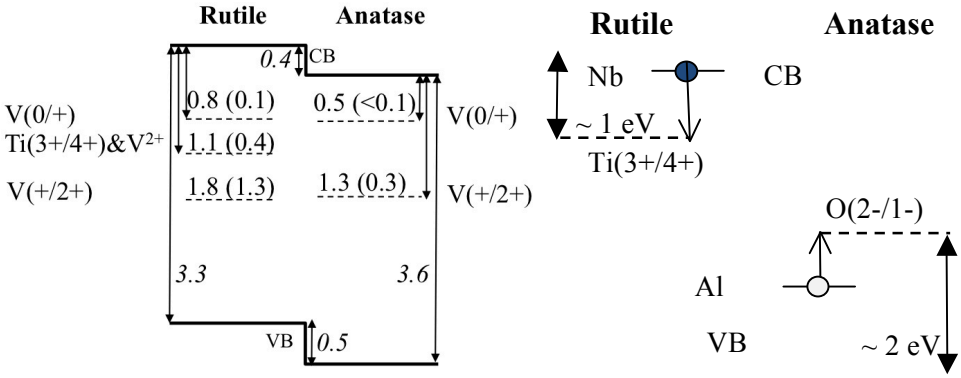

Figure 2: a) Vertical (adiabatic) charge transition levels (in eV), related to the oxygen vacancy in rutile and in anatase. The single particle band gaps are aligned following the results of Ref. [3]. The rutile results resolve the long existing controversy between observed IR transitions in strongly reduced samples (see Fig.1b), and the electron spectroscopy and paramagnetic spectroscopy results in more oxidized samples. The former give 1.2 (0.4) eV [A. K. Gosh et al. Phys. Rev. **184**, 979 (1969)], while the latter indicate an adiabatic transition level below 0.1 eV for the triplet state of the vacancy [F. D. Brandao et al. Phys. Rev B **80**, 235204 (2009)], which is also responsible for the vertical transition at 0.8 eV.

The electron self-trapping nature of rutile is also confirmed by direct experiments, with a vertical transition energy of ~0.3 eV [I. R. MacDoald et al. J. Photochem. Photobiol. A **216**, 238 (2010); D. A. Panyatov et al. J. Phys. Chem. C **116**, 4535 (2012)]. In defect-free rutile we calculate a vertical transition energy of 0.5 eV for the Ti(4+/3+) native trap. In contrast to rutile, such electron traps do not occur in anatase. Instead, holes get trapped by an O(2-/1-) transition. Our calculation for the recombination of an exciton, with the hole trapped at such a site, gives 2.26 eV, in very good agreement with the experimentally observed 2.15 eV [T. Sekiya et al. J. Lumin. **87-89**, 1140 (2000)]. Our discovery of the different carrier self-trapping effects in rutile and anatase has allowed us to explain the differences observed between them for Nb- and Al-doping. As Fig.2b shows, Nb is a shallow donor in anatase but autoionizes into native electron traps in rutile, while the opposite is true for the hole in case of Al doping. This explains why only anatase can be used as an *n*-type transparent conducting oxide (TCO), and has serious consequences for other electronic and optoelectronic applications (for details see Ref. [4]).

We have investigated the Nb- and Ta-doping of anatase for TCO purposes. Besides transparency, the primary goal in this application is to achieve high conductivity. The latter is influenced by the change of the (optical) effective mass with carrier concentration. We have shown that HSE06 is capable to reproduce this dependency quantitatively, and that Ta causes a smaller anisotropy in the effective mass [6,7]. In combination with the higher solubility under oxygen-pure growth conditions, the smaller effective mass of Ta could lead to higher conductivities than Nb, which has been dominantly used so far.

The band alignment between rutile and anatase, as shown in Fig.2, have been calculated

both by using the charge neutrality levels of the bulk material [3] and by simulating a rutile(100) –anatase(100) interface directly [8] Our results are supported by experiment [G. Xiong et al., Adv. Funct. Nanomater. **17**, 2133 (2007); L. Kavan, M. Grätzel et al. J. Am. Chem. Soc. **77**, 347 (1998)]. In combination with the self-trapping effects, this alignment indicates that in mixed powders, mobile holes are dominant in rutile, while mobile electrons in anatase. This charge separation explains the increased photocatalytic activity of mixed powders.

Besides interface studies, we have also investigated chemical reactions on the anatase (101) surface [9,10]. We have shown that, in contrast to the rutile (110) surface, where the oxidation of CO is assisted by electrons [Z. Zhang and J. T. Yates, Jr., J. Am. Chem. Soc. **132**, 12804 (2010)], this is a hole assisted process on the anatase (101) surface, with the possibility of cyclic repetition, i.e. photocatalysis.

Finally, we have extended our investigations to nanostructures. Anatase and rutile both lend themselves easily to nanostructuring. Anatase [001] nanowires could be grown with diameters as small as 1 nm [Ch. Liu and Sh. Yang, ACS Nano, **3**, 1025 (2009)]. We have shown that in this size range, wires with a screw axis are energetically preferred and, indeed, the simulated electron microscopic image of such a structure agrees with the actually observed one [11]. We have also found that anatase [001] wires with a screw axis symmetry posses massless, quasi-relativistic Dirac-states in the conduction band [12]. As it is known from the physics of graphene and topological insulators, such states have very high mobility. However, those systems are semi-metals, which makes their application in electronic switching devices difficult, because of a low on-off current ratio. In anatase nanowires, however, the empty Dirac-states are near to the fundamental band gap, and could be populated by a gate voltage as shown in Fig. 3.

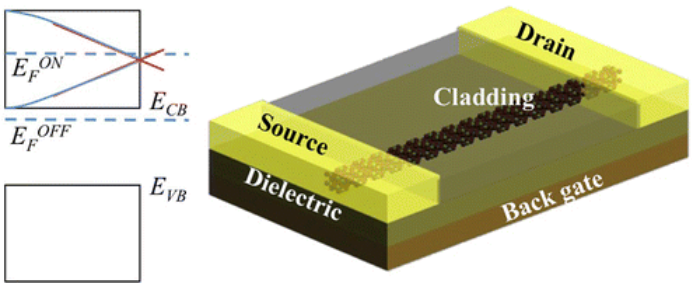

Figure 3: Scheme of a FET device, based on a gate-voltage induced insulator to Dirac-material transition in anatase nanowires. The device is fabricated with a back gate to switch it between the ON and OFF states. When no back gate voltage is applied, the Fermi energy (E_F) lies below the conduction band minimum and the device is in the OFF state. When a back gate voltage is applied, E_F is shifted to the vicinity of the Dirac-point.

Such a device would allow a channel mobility of 10^4 - 10^5 cm^2/Vs (higher than in semiconductor nanowires) and an on-off ratio of $3 \cdot 10^3$ - $3 \cdot 10^5$ (much better than in graphene-based devices).

In summary, the HLRN grant hbc00001 has allowed us to publish 12 papers (see Refs. [1-12]) based on 3 years' work. Our methodology paper published in 2010 has brought 27 citations in 3 years (impact factor 9), and the 6 application papers published in 2011 were cited 42 times so far (average impact factor 3.5). We have been invited to present our results

at a CECAM workshop in Lausanne and both at the 242nd and 246th Natl. Meeting of the American Chemical Society (2011 and 2013, resp.). The recognition of our results by the international community has helped us to bring a CECAM workshop on TiO_2 to Bremen in 2010 [13]. We would like to express or appreciation to HLRN for that and to thank all the staff (but especially B. Kallies and G. Gauss) for their help.

References:

[1] P. Deák, B. Aradi, T. Frauenheim, E. Janzén, and A. Gali, *Accurate defect levels obtained from the HSE06 range-separated hybrid functional*.
Phys. Rev. B **81**, 153203 (2010).

[2] P. Deák, A. Gali, B. Aradi, and T. Frauenheim, *Accurate gap levels and their role in the reliability of other calculated defect properties*. in "Advanced calculations for defects in materials", eds. A. Alkauskas, P. Deák, J. Neugebauer, A. Pasquarello, and C. G. Van de Walle
[Wiley-VCH, Berlin 2011] pp. 139-154; online at DOI: 10.1002/pssb.201046210

[3] P. Deák, B. Aradi, and T. Frauenheim, *Band lineup and charge carrier separation in mixed rutile-anatase systems.*
J. Phys. Chem. C, **115**, 3443 (2011).

[4] P. Deák, B. Aradi, and T. Frauenheim, *Polaronic effects in TiO_2 calculated by the HSE06 hybrid functional: Dopant passivation by carrier self-trapping.*
Phys. Rev. B **83**, 155207 (2011).

[5] P. Deák, B. Aradi, and T. Frauenheim, *Quantitative theory of the oxygen vacancy and carrier self-trapping in bulk TiO_2.*
Phys. Rev. B **86**, 195206 (2012).

[6] H. A. Huy, B. Aradi, T. Frauenheim and P. Deák, *Calculation of carrier-concentration-dependent effective mass in Nb-doped anatase crystals of TiO_2.*
Phys. Rev. B **83**, 155201 (2011).

[7] H. A. Huy, B. Aradi, T. Frauenheim and P. Deák, *Comparison of Nb- and Ta-doping of anatase TiO_2 for transparent conductor applications.*
J. Appl. Phys. **112**, 016103 (2012).

[8] P. Deák, B. Aradi, H. A. Huy, and T. Frauenheim, *Band-lineup between rutile and anatase.*
ACS 242nd Natl. Meeting, Abstract: 274-COMP (2011).

[9] R. Wanbayor, P. Deák, T. Frauenheim, V. Ruangpornvisuti, *First principles theoretical study of the hole-assisted conversion of CO to CO_2 on the anatase TiO_2(101) surface*
J. Chem. Phys. **134**, 104701 (2011).

[10] R. Wanbayor, P. Deák, T. Frauenheim and V. Ruangpornvisuti, *First-principles investigation of adsorption of N_2O on the anatase TiO_2 (101) and the CO pre-adsorbed TiO_2 surfaces*.
Comput. Mater. Sci. **58**, 24-30 (2012).

[11] B. Aradi, P. Deák, Huynh Anh Huy, A. Rosenauer, and T. Frauenheim, *The role of symmetry in the stability and electronic structure of titanium dioxide nanowires*.
J. Phys. Chem. C **115**, 18494 (2011).

[12] P. Deák, B Aradi, A. Gagliardi, H. A. Huy, G. Penazzi, B. Yan, T. Wehling, and T. Frauenheim, *Possibility of a Field Effect Transistor Based on Dirac Particles in Semiconducting Anatase-TiO_2 Nanowires.*
Nano Letters **13**, 1073-1079 (2013).

[13] Intl. CECAM workshop (Bremen 2010) on Titania at:
http://www.bccms.uni-bremen.de/index.php?id=1839

6.2 hbc00012: **All-atom moleculardynamic investigations of the adhesion mechanisms at the contact interface of TiO_2 nanoparticles in films and aggregates**

HLRN-Projektkennung:	hbc00012
Laufzeit:	IV/2012 – III/2013
Projektleiter:	Prof. Dr. Lucio Colombi Ciacchi
Projektbearbeiter:	Prof. Dr. Lucio Colombi Ciacchi Jens Laube
Institut / Einrichtung:	Hybrid Materials Interfaces Group, Faculty of Production Egineering and Bremen Center for Computational Materials Science, University of Bremen

Overview

Controlling the agglomeration or dispersion behavior of nanoparticles is important in a number of technical applications such as catalysis, sensorics and hybrid materials synthesis. To this aim, a deep understanding of the nature of the contact forces and the adhesion mechanisms between nanoparticles is essential. It is generally agreed that capillary forces dominate adhesion in the case of hydrophilic surfaces and humidity levels higher than about 70% [1,2], and the experiments can be well interpreted by means of continuum capillary models, albeit of considerable complexity [3].

Only recently it was realized that the humidity dependence of the adhesion force is determined sensitively by the structure of the interacting surface on the 1 nm scale. With decreasing particle size, it is expected that effects arising from the atomic-level structure of the particle-particle interfaces start playing a governing role on their adhesion behavior. This calls for further developments in both experimental techniques and theoretical modeling for a more complete characterization of particle-particle or particle-substrate adhesion mechanisms.

To provide a comprehensive view of the influence of the local surface-structure at the contact-point, in this work, adhesion forces are analysed by all-atom Molecular Dynamics (MD) simulations for different orientations of rutile particles. The deviations of adhesion-forces at different particle-orientations shall help understanding the fluctuations appearing in AFM-experiments. According to the results of Ketteler et al. [4], the amount of water molecules adsorbed per surface-area on rutile 110-surfaces depends on the relative air humidity. This dependence will be used to differentiate between the capillary-part and the structure-dependend-part of the adhesion forces experimentally and theoretically.

Methods

Particle models for the simulations are generated by carving a spherical portion out of extended rutile single crystals. The resulting free surfaces are then annealed in classical MD simulations and the undercoordination defects (less than fivefold-coordinated Ti atoms) are saturated with terminal OH groups. A number of H atoms equal to the number of OH atoms is then placed on terminal O atoms to ensure charge neutrality. Furthermore, defined

amounts of physisorbed water molecules are placed over the particles' surface to simulate conditions of different humidity.

The MD simulations are carried out using the LAMMPS program package [5] in an NVT-Ensemble at 300K constant temperature. The integration time step amounts to 2 fs. Within the oxide crystal, the interactions are described by a modified form [6] of the force field of Matsui and Akaogi [7]. The interactions of crystal- TiO_2 atoms with adsorbed free water are computed by a potential developed by Schneider et al. [8] for TIP3P [9] water molecules.

Force-displacement curves between two particles are computed in a series of MD simulations, where two particles are constrained to a certain center-of-mass separation. In these simulations the atoms belonging to the oxide crystals are fixed and the contact forces are calculated as the average force acting on each crystal core. Each simulation lasts 2.5 ns including a 0.5 ns equilibration period, which is discarded from the analysis.

Current Results

Force-displacement curves for the detachment of a particle-model at approximately 50 % air-humidity were calculated in an earlier project phase [10]. The calculated curves for the detachment of these particles, shown in figure 1, reveal, as expected, a long-range capillary force arising from a water neck building up in the interparticle region. However, at low distances, the forces present a characteristic oscillatory behaviour due to the structuring of water layers in surface proximity, as can be seen from simulation-trajectories. The force-oscillations show a well-defined maximum adhesion force of the order of a few nN, in agreement with AFM-force-spectroscopy-measurements performed on TiO_2-agglomerates with primary particle diameters of 12nm.

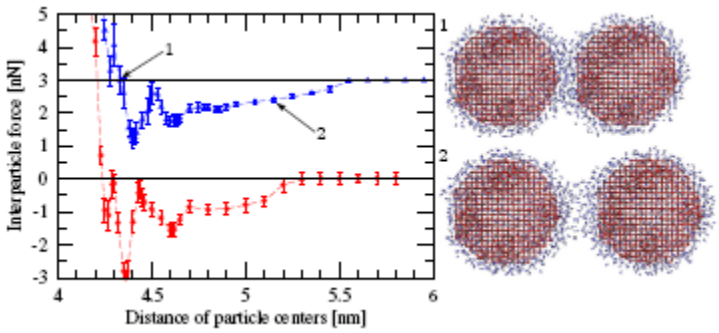

Figure 1: Computed force-distance curves for anatase (blue) and rutile (red) TiO_2 nanoparticles bearing a water coverage of 11 molecules/nm², as obtained from constrained MD simulations, along with two representative snapshots corresponding to contact at equilibrium (1) and attraction due to a capillary water neck (2). The forces between anatase particles are shifted by +3 nN for clarity [10].

Figure 2 (left) shows the development of the interparticle forces with rising amounts of physisorbed water-molecules on the particle-surface. As can be seen, increasing the amount of surface-adsorbed water molecules on the particles (depending on the air-humidity) leads to a change in the capillary behaviour, while the oscillations remain the same. For higher humidities, the absolute values of the capillary forces decrease, while the capillary neck forms also for higher distances until in bulk water only the pure force-oscillations remain.

In the simulation trajectories, the capillary neck is observed to be build from adsorbed water between the particles. Capillary geometries can now be extracted from this neck and are used to calculate the capillary forces between the two nanoparticles. A comparison of the

capillary forces calculated in this manner to the forces calculated directly from the simulations in the capillary region shows very good agreement.

In Figure 2 (right) the development of the maximum adhesion force in the force-displacement-curves is plotted against the number of physisorbed water. If the capillary force calculated from the capillary geometries at the same distance is substracted from the maximum value, the resulting difference is constant over the different humidities and close to the value in bulk water where no capillary forces exist. This suggests that the adhesion forces between nanoparticles can be simply divided into two separate force components. One depending on the local water-structuring between the two particles leading to well defined force oscillations and the other describing the capillary forces between the particles caused by the capillary effect of the water adsorbed to the surface.

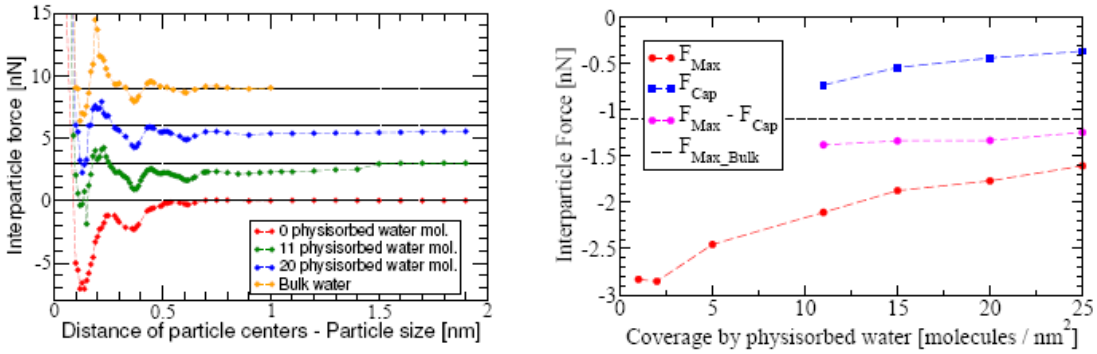

Figure 2: Computed force-distance curves for different amounts of physisorbed water (left) and development of maximum force value from force-displacement curves and corresponding capillary forces plotted over the number of physisorbed water molecules (right)

Outlook

In the next stage of this project, different particle orientations of the two particles facing each other shall be investigated to further study the influence of the local water structure on the force-oscillations.

Funding

This Project is funded by the DFG in the Schwerpunktprogramm 1486 "Partikel im Kontakt (PIKO) - Mikromechanik, Mikroprozessdynamik und Partikelkollektive "

References

[1] W.Q. Ding. Micro/nano-particle manipulation and adhesion studies. *Journal of Adhesion Science and Technology*, 22:457–480, 2008.
[2] S. Yang, H. Zhang, M. Nosonovsky, and K.H. Chung. Effects of contact geometry on pull-off force measurements with a colloidal probe. *Langmuir*, 24(3):743–748, 2008.
[3] M. Farshchi-Tabrizia, M. Kappl, and H.J. Butt. Influence of humidity on adhesion: An atomic force microscope study. *Journal of Adhesion Science and Technology*, 22:181–203, 2008.
[4] G. Ketteler, S. Yamamoto, H. Bluhm, D. E. Andersson, K. Starr, F. Ogletree, H. Ogasawara, A. Nilsson, and M. Salmeron. The nature of water nucleation sites on

tio2(110) surfaces revealed by ambient pressure x-ray photoelectron spectroscopy. *J. Chem. Phys.*, 111:8278–8282, 2007.
[5] S. Plimpton. Fast parallel algorithms for short-range molecular dynamics. *Journal of Computational Physics*, 117:1–19, 1995.
[6] J. Schneider and L. Colombi Ciacchi. First principles and classical modeling of the oxidized titanium (0001) surface. *Surface Science*, 604:1105–1115, 2010.
[7] M. Matsui and M Akaogi. Molecular dynamics simulation of the structural and physical properties of the four polymorphs of tio2. *Molecular Simulation*, 6:239–244, 1991.
[8] J. Schneider and L. Colombi Ciacchi. A classical potential to model the adsorption of biological molecules on oxidized titanium surfaces. *J. Chem. Theory Comput.*, 7:473–484, 2011.
[9] W.L. Jorgensen, J. Chandrasekhar, J.D. Madura, R.W. Impey, and M.L. Klein. Comparison of simple potential functions for simulating liquid water. *J. Chem. Phys.*, 79:926–936, 1983.
[10] S. Salameh, J. Schneider, J. Laube, A. Alessandrini, P. Facci, J.W. Seo, Ciacchi L., and M¨adler L. Adhesion mechanisms of the contact interface of tio2 nanoparticles in films and aggregates. *Langmuir*, Accepted Manuscript:0–24, 2012

6.3 hbi00014: Modelling turbulent heat transfer of a Rayleigh- Bénard problem with compressible Large-Eddy simulation

HLRN-Projektkennung:	hbi00014
Laufzeit:	I/2011 – III/2012
Projektleiter:	Dr. Rodion Groll
Projektbearbeiter:	Claudia Zimmermann
Institut / Einrichtung	ZARM, Center of Applied Space Technology and Microgravity, University of Bremen

Overview

A Rayleigh-Bénard problem describes thermally driven flows against gravity between two heat-controlled plates. The compressible fluid is accelerated by local density differences and the resulting pressure gradient. In close proximity to the heated walls the temperature distribution is determinate by increasing temperature gradients. In the centre region the heat transfer is defined by convective mass exchange. This transfer generates turbulent shear layers parallel to the direction of gravity. In these layers hot lift-streams and cold sink-streams increase the intensity of turbulence. This unsteady behaviour dominates the vertical heat flux. This is illustrated for a natural convection flow in a closed container in figure 1. It shows the instantaneous temperature iso-surfaces after 380 s.

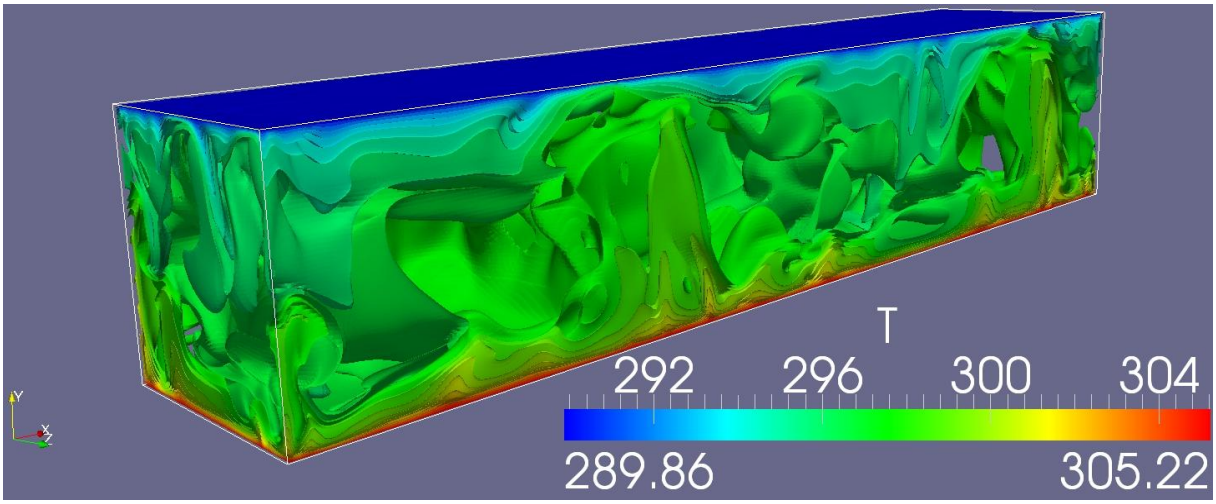

Figure 1: Instantaneous temperature iso-surfaces in the closed container for a Rayleigh-number of $Ra = 1.92 \,.\, 10^8$ after 380 *s*

Natural convection flows are caused for example in the atmosphere by solar radiation and can effect hurricanes. Furthermore they are used for cooling systems in technical setups instead of fans to reduce noise exposure and technical failures.

Numerical simulation

To investigate the turbulent flows the numerical simulations are compared with a suitable experimental setup of [1]. As test case a rectangular, air-filled container with an aspect ratio of $\Gamma = \frac{L}{H} = 5$ is chosen as it is shown in figure 1. The walls are smooth and the horizontal ones are heated homogeneously with a constant temperature difference ΔT. Lateral walls are adiabatic with $\frac{\partial T}{\partial y}\,|_{y=0} = 0$. The velocity field at the walls is zero due to a non-slip-condition $(\boldsymbol{u} \equiv 0)$. Because of transient turbulence and high local density gradients, a Large Eddy simulation (LES) with a compressible coupled model is highly suited for the numerical discretisation. Previous work investigates similar setups with a Boussinesq-approximation [3].

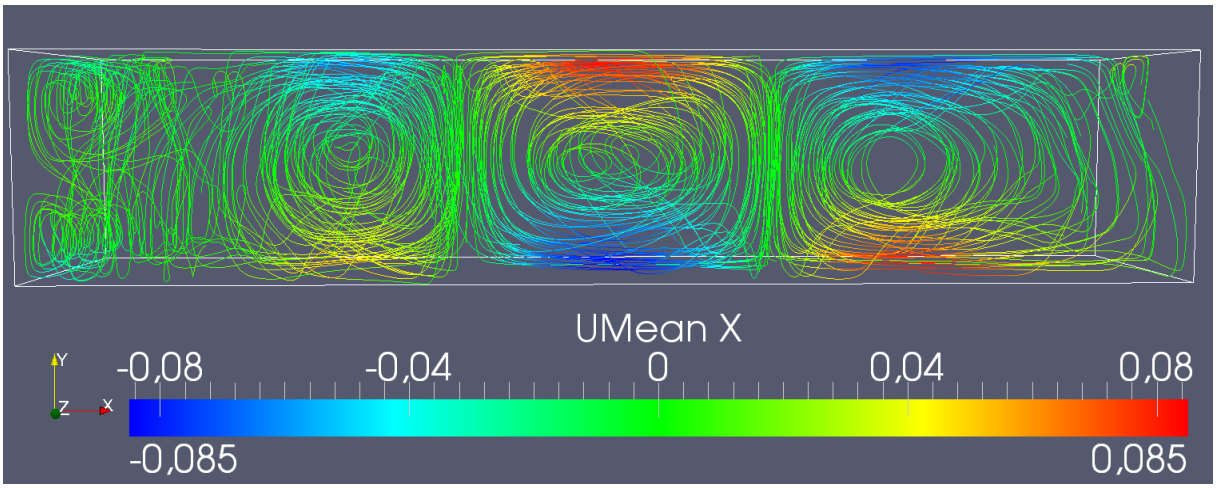

Figure 2: Mean horizontal velocity profile at the xy-midplane in the closed container for a Rayleigh-number of $Ra = 1.92 \cdot 10^8$ after 380 *s*

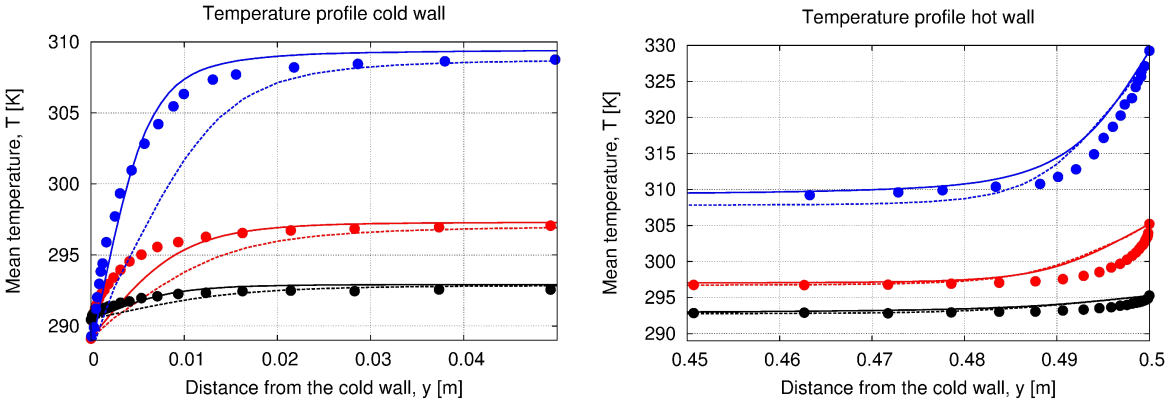

Figure 3: Temperature profile at the cold (left) and hot (right) wall for the Rayleigh-numbers: Ra=4.1 $\cdot 10^8$ (blue), Ra=1.92 $\cdot 10^8$ (red) and Ra=6.16 $\cdot 10^7$ (black), **-** fine simulation grid (140x140x430) cells **- -** coarse simulation grid (50x50x150) cells, • study [1]

For the LES the flow is separated in large and small scales, the so-called sub-grid scales. The large scales are solved directly on the discretisation grid, while the sub-grid scales are modelled with an applicable turbulence model. This reduces essentially the required computing time. The chosen turbulence model of Fureby [2] is based upon a compressible Smagorinsky-model. The turbulent structures are developed mainly directly close to the temperatured walls. Hence, an adequate fine resolution must be chosen in this region. The

discretisation grid of the simulation consists of approximately 8 million cells. Therefore, a high computer performance and the possibility of parallelisation in several hundreds processes is essential for the simulation. The LES is used in the open-source software Open-FOAM® at the HLRN.

The main focus of the numerical investigation are the temperature and velocity distributions in the vicinity of the temperatured walls for different parameters like the Rayleigh-number and different grid resolutions. The Rayleigh-number characterises the heat flux through the particular flow layers. The investigated Rayleigh-numbers lie between $6 \cdot 10^7$ and $4 \cdot 10^8$. The mean horizontal velocity at the xy-midplane after 380 s shows the typical convection cells which are developed between the temperature-controlled walls (s. figure 2). The temperature gradients are plotted for two different grid resolutions and three Rayleigh-numbers at the hot and cold wall in figure 3 against the experimental data of [1]. The gradients directly at the walls are smaller and not anti-symmetrical like in the experimental results. This could be due to a higher wall heat flux or a more intense mixing of hot and cold streams in the experiment. The importance of a sufficient fine grid resolution can clearly be seen at the cold wall. In the bulk of the container both simulation results approach the experimental data.

Outlook

The next step in the future work will be the investigation of the hydrodynamic stability of the turbulent natural convection. Therefore a modal analysis will be conducted. Additionally the stabilizing effect of the Coriolis acceleration is tested. Subsequent the results of further LES will be validated by the data of a suitable experiment in a huge-scale centrifuge.

References

1. Ebert, C. Resagk and A. Thess. Experimental study of temperature distribution and local heat flux for turbulent Rayleigh-Bénard convection of air in a long rectangular enclosure. *Int. J. of Heat and Mass Transfer*, **51**: 4238-4248, 2008.
2. C. Fureby. On subgrid scale modeling in large eddy simulations of compressible fluid flow. *Physics of Fluids*, **8** (5): 1301-1311, 1996.
3. O. Shishkina and A. Thess. Mean temperature profiles in turbulent Rayleigh-Bénard convection of water. *J. of Fluid Mechanics*, **633**: 449-460, 2009.

Conference proceedings

Groll, R., Zimmermann, C., Rath, H. J. *Compressible Large-Eddy Simulation of Boundary-Layer Heat Transfer in a Turbulent Convective Flow*, 83rd Annual Meeting of the International Association Applied Mathematics and Mechanics (GAMM), Darmstadt, Germany (2012)

Zimmermann, C., Groll, R, Rath, H.J.: *"Kompressible Large-Eddy-Simulation thermischer Wandgrenzschichten in turbulenten Konvektionsströmungen"*, 128. Norddeutsches Mechanikkolloquium, Berlin, Germany (2011)

Zimmermann, C., Groll, R. und Rath, H. J.: *Development of an experimental set-up describing turbulent convective flows driven by atmospheric temperature layers*, Proceedings of the 38th scientific assembly of the Committee on Space Research (COSPAR), Bremen, Germany (2010)

Support

The projekt is funded by the "Zentrale Forschungsförderung" of the University Bremen, project "TurboTherm". The HLRN supports the project totally with 70kNPL. The authors wish to thank Dr. C. Resagk from the Ilmenau University of Technology for providing the experimental data of [1].

6.4 hbi00015: Numerical Large Eddy Simulation of a turbulent flow in a spherical gap

HLRN-Projektkennung: hbi00015
Laufzeit: III/2011 – III/2013
Projektleiter: Dr. Rodion Groll
Projektbearbeiter: K. Leach
Institut / Einrichtung: ZARM, Center of Applied Space Technology and Microgravity, University of Bremen

Abstract

- Design and simulation of a new kind of miniature abrading sphere which is magnetically mounted inside a spherical gap and set in rotation pneumatically with air.
- Large Eddy Simulation is performed in conjunction with the compressible Smagorinsky model according to Fureby [1]. Minimal temperature variation allows for the assumption of adiabatic walls. Fluid-solid interaction is modeled using the law of the wall for compressible turbulent flow [2].
- A parametric study is done to determine optimal geometric layout while taking physical restrictions into account. The resulting optimal configuration is then examined in detail in order to determine demands to be met by the computerised control of the magnetic bearing as well as to quantify the force available to the abrasion process.
- Finally, a mathematical relation is obtained that determines available abrasion force depending on standard volumetric flow rate and rotation frequency.

Motivation

Miniaturisation is of great importance in many fields such as mechatronics, optics, or medicine as it enables new functionality or makes processes more economical. While increasing precision has made it possible to produce smaller and smaller workpieces, the tools used to work on them have, for the most part, remained constant in size. The skewed ratio of tool size to workpiece size creates a growing ecological, economic and technical inefficiency regarding respective processes. Until now, miniaturising existing tools was performed in order to combat this skewed ratio. This approach is, however, reaching its limits regarding technical feasibility and usefulness. For this reason, new innovative concepts and tools need to be developed in order to advance in the field of miniaturisation.

Since the ratio of surface to volume increases dramatically with increasing miniaturisation, one has, proportionally, far more functional surface to work with as volume decreases. This effect is extremely useful for abrasive tools, as the control dynamics improve with deceasing tool size, thus also improving the tools ability to adapt to particular machining conditions. Most abrasive tools used to create micro cavities suffer from the following problem: since the axis of rotation and its orientation to the workpiece are crucial in ensuring positive grinding results, aligning the axis of rotation is key when grinding a cavity. A grinding pencil, for instance, has its theoretical maximum effectiveness when the axis of rotation is parallel to the work piece. This, however, is not always practical since the grinding pencil's mounting apparatus could touch down on to the workpiece. Furthermore, should the axis of rotation be perpendicular to the workpiece, the grinding pencil's abrasion would tend to zero. This

problem can be countered by tilting the apparatus slightly, however, this still delivers mediocre results at best. Figure 1 depicts the problems stated along with a theoretical solution in which the axis of rotation is parallel to the workpiece at all times, thereby maximising the tool's effectiveness. It is the goal of project GrindBall to develop such a tool, which, in addition, combines propulsion and control into one single element.

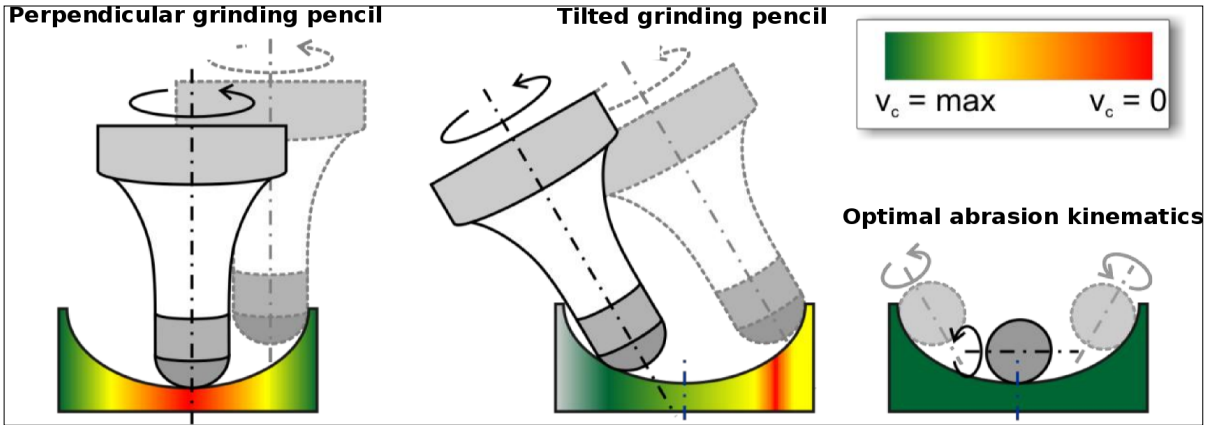

Figure 1: Grinding speed $\mathbf{v}_c$ depending on axis orientation (picture courtesy of the Laboratory for Precision Machining (LFM))

Basic setup

To achieve the objectives stated above, fluid driven propulsion is used in conjunction with a ferromagnetic sphere covered in an abrasive coating. The repelling force exerted by the fluid is compensated by an adjustable opposing force generated by a magnetic bearing so that the sphere is held in a fixed relative position at all times.
The first prototype will utilise a sphere with a diameter of 40mm. Throughout the duration of the project, this diameter is to be gradually scaled down to 4mm with surrounding elements shrinking in proportion.
The force necessary to achieve abrasion is applied via fluid flow by setting the sphere in rotation. Due to the sphere having little mass and its resulting low moment of inertia, high rotational frequencies and an extremely high control dynamic are to be expected. Planning and construction of the GrindBall requires interdisciplinary cooperation between production technology, electrical engineering, and fluid mechanics.

Simulation framework

Simulations are conducted using the OpenCFD package OpenFOAM-2.0.1. Mach numbers between 0.1 and 0.9 as well as Reynolds numbers ranging from 10^3 to 10^5 justify the use of compressible Large Eddy Simulation (LES) in conjunction with the compressible Smagorinsky model according to Fureby [1]. Specifically, transport equations are solved using the pressure-based finite volume solver `rhoPimpleFoam`. Pressure and density are linked via the Ideal Gas Law [2]. The temperature dependance of viscosity is modeled according to Sutherland's viscosity model [2]. Minimal temperature variation allows for the assumption of adiabatic walls. Finally, fluid-solid interaction is modeled using the Law of the Wall [2].

Preliminary results

First, a parametric study is conducted in order to identify an optimal geometric configuration for the tool. The resulting optimal setup is subsequently simulated and analysed in detail to determine the demands to be met by the magnetic bearing and the force effectively available

to the abrasion process. Furthermore, a mathematical relation governing the behaviour of the available abrasion force is derived.

1. Parametric Study

The goal of the parametric study is to make the GrindBall as efficient as possible while abiding to certain practical and physical restrictions. Geometric features are varied in an attempt to maximise abrasion force available to the tool while maintaining a stable state of operation easily manageable by the magnetic bearing. Once found, the optimum geometric layout is subjected to a detailed analysis.

2. GrindBall Prototype

The resulting optimum setup is subjected to a series of simulations with a variety of mass flow rates and rotation frequencies of the sphere. Pressure forces acting on the sphere are determined in order to ascertain demands to be met by the magnetic control element prior to its construction. Forces available to the process of abrasion are examined in detail. Individual relations are established between flow rate, rotation frequency and abrasion force. These individual relations are then combined into a single three-dimensional relation governing abrasion force as a function of rotation rate and flow rate (see Figure 2). The results obtained for this first prototype are vital for further development of the tool.

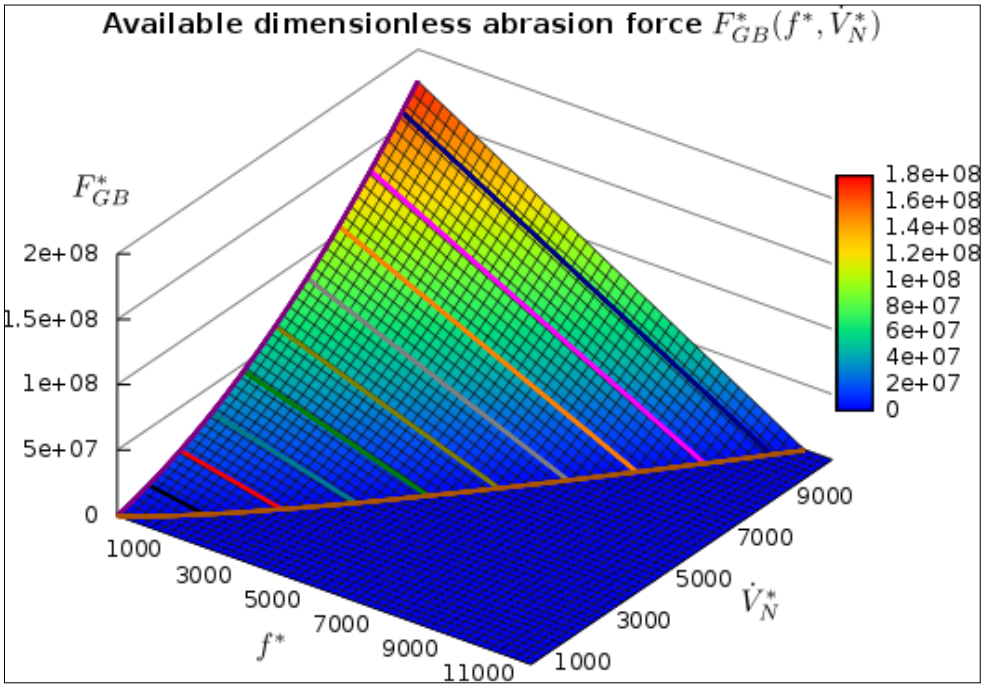

Figure 1: Dimensionless force F^*_{GB} available to the abrasion process in terms of dimensionless rotation frequency f* and dimensionless standard volumetric flow rate V^*_N

Outlook

The main focus of future work on this project is scaling down the tool. The first objective is a diameter of 8mm for the grinding sphere with surrounding elements shrinking in proportion. Several parametric studies are to be conducted regarding the choice of a suitable propulsion medium and optimum geometric layout. Once found, the dynamics of the new geometry are to be analysed in great detail prior to construction and use of the actual tool. Influence of

surface coating on the tools performance is to be simulated and analysed. Once the previously mentioned goals are achieved, further miniaturisation is to be performed, most likely to 4mm. In addition, several publications are to be made on this topic.

Adequately determining pressure and viscous forces requires extremely fine computational grids which in turn require access to parallel super-computers. Accurate work on this project would not be possible without access to the super-computing facilities provided by the HLRN.

References

[1] C. Fureby. On subgrid scale modeling in large eddy simulations of compressible fluid flow. *Physics of Fluids*, 8:1301–1311, 1996.

[2] F.M. White. *Viscous Fluid Flow*. McGraw-Hill, 1991.

Sponsorship

This project is sponsored by the German Research Foundation (DFG) as part of the work-group Small Machine Tools (SPP 1476) and supported by the North-German supercomputing alliance (HLRN) with 40kNPL.

6.5 hbk00018: Berechnung der Wasserdampfkonzentrationen aus Limb-Messungen des Satelliteninstrumentes SCIAMACHY

HLRN-Projektkennung:	hbk00018
Laufzeit:	I/2012 – IV/2013
Projektleiter:	Prof. Dr. J. P. Burrows
Projektbearbeiter:	Wolfhardt Lotz, Alexej Rozanov, Marco Vountas, Katja Weigel
Institut / Einrichtung:	Institut für Umweltphysik, Universität Bremen

1 Übersicht

- SCIAMACHY (engl.: Scanning Imaging Absorption spectroMeter for Atmospheric CHartographY), ein Instrument auf dem Europäischen Satelliten Envisat, hat die Erde zwischen August 2002 und April 2012 beobachtet.
- Wir berechnen den Wasserdampf oberhalb der Wolken, d.h. in der oberen Troposphäre und unteren Stratospheräre aus horizontsondieren Messungen von SCIAMACHY
- Der Wasserdampf dort spielt, als natürliches Treibhausgas, eine wichtige Rolle für das Klima und de Zirkulation in der Atmosphäre
- Mit Hilfe der Rechnungen auf dem HLRN haben wir eine fast 10 Jahre lange Wasserdampf-Zeitreihe berechnet und können damit zur Initiative SPARC-DI (engl.: Stratospheric Processes and their Role in Climate) beitragen.
- Dieser Datensatz ist ein Ergebins der ersten Phase des DFG-Projektes SHARP (engl.:Stratospheric Change and its Role for Climate Prediction) und des ESA-Projektes SPIN (engl: ESA SPARC Initiative)
- Wegen der Menge der Profile und weil zur Berechnung des Wasserdampfs aufwändige Strahlungstransportrechnungen nötig sind, ist der Rechenzeitbedarf dabei groß. Deshalb wurde bisher nur jeder 8. Tag global und jeder 2. Tag zwischen 45°S und 45°N ausgewertet.
- Weitere Rechnungen sind nötig um den Datensatz zu vervollständigen und mögliche Verbesserungen zu testen.

2 Wasserdampf über den Wolken

Wasser gibt es in der Atmosphäre nicht nur als Regen, Schnee und in Form von Wolkentröpfchen und Eiskristallen, sondern auch als Wasserdampf. Der ist durchsichtig, das heißt wir können ihn mit unseren Augen nicht sehen, weil Wassermoleküle wenig sichtbares Licht absorbieren. Im Gegensatz dazu absorbieren Wassermoleküle im langwelligeren, infraroten Bereich des Spektrums besonders viel Strahlung. Diesen Bereich können wir nicht mit bloßem Auge sehen, eine Wärmebildkamera kann ihn aber beispielsweise sichtbar machen. Trotzdem spielt er für die Strahlung in unserer Atmosphäre eine wichtige Rolle: Er lässt das sichtbare Licht, dass von der Sonne kommt ungehindert zum Boden durch, absorbiert aber viel Strahlung im infraroten Bereich und damit die von der Erde emittierte Wärmestrahlung. Das macht den Wasserdampf zum wichtigsten natürlichen Treibhausgas in unserer Atmosphäre. Den meisten Wasserdampf findet man nahe des Erdbodens, aber selbst oberhalb der Wolken gibt es noch Wasserdampf. Modellstudien haben gezeigt, dass

auch er in diesem Höhenbereich, der oberen Troposphäre und untere Stratosphäre, einen deutlichen Einfluss auf unser Klima am Boden hat. Wie groß dieser Einfluss genau ist, hängt dabei von der Menge des Wasserdampfes in der Luft ab. Diese wird häufig als Volumenischungsverhältnis zwischen Wasserdampf und "trockener" Luft in Teilen pro Million [ppmV] angegeben.

Dieses Mischungsverhältnis variiert je nach Ort und Zeit stark. Deshalb ist es ein Ziel des DFG Projektes SHARP (siehe auch: www.fu-berlin.de/sharp/) zu einem besseren Verständnis der Verteilung und der zeitlichen Änderung des Wasserdampfgehaltes in der Atmosphäre und dessen Wirkung auf das Klima beizutragen. Dazu braucht man möglichst globale, regelmäßige und dichte Messungen des Wasserdampfs. Solche Messungen oberhalb der Wolken gibt es vor allem von Satelliten. Wir arbeiten daran im Rahmen von SHARP eine Zeitserie der zonal gemittelten Wasserdampfmischungsverhältnissen aus Messungen von SCIAMACHY (engl.: Scanning Imaging Absorption spectroMeter for Atmospheric CHartographY) ab August 2002 bereitzustellen.

SCIAMACHY ist ein Spektrometer auf dem europäische Satellit ENVISAT. SCIAMACHY MEssungen gibt es seit August 2002 bis zum plötzlichen Kontaktverlust mit Envisat im April 2012. Um Informationen aus verschiedenen Höhen in der Atmosphäre zu bekommen sind Limb-Messungen von SCIAMACHY besonders gut geeignet. Bei diesem Messmodus schaut das Instrument durch die Atmosphäre über den Erdboden hinweg in Richtung des Weltraumes. Dabei wird f\"{u}r Höhenstufen von jeweils 3.3 km ein Spektrum des gestreuten Sonnenlichts gemessen. Aus diesen Spektren berechnen wir Wasserdampfprofile im Höhenbereich zwischen 11 km und 23 km.

Wie kommt man von der gemessenen Strahlung zu Wasserdampfprofilen?
Dazu werden die charakteristischen Absorbtionen der Wassermoleküle im infraroten Bereich des Spektrums genutzt. SCIAMACHY misst das gestreute Sonnenlicht in der Atmosphäre. Auf dem Weg zum Instrument absorbiert der Wasserdampf einen Teil der Strahlung, so dass man Absorbtionslinien im gemessenen Spektrum sieht. Vereinfacht gesagt, verrät die Position der Linien, welche Gase sich in der Atmosphäre befinden. Die Linienstärke spiegelt die Konzentration der jeweiligen Gase wieder. Allerdings spielen auch noch andere atmosphärische Größen, zum Beispiel Druck und Temperatur, eine Rolle. Deshalb kann man nicht direkt aus den Spektren auf die Wasserdampfprofile schließen. Um alle Einflüsse richtig berücksichtigen zu können, berechnen wir mit dem Strahlungstransportmodel SCIATRAN aus einer gegebenen Atmosphärenzusammensetzung die Strahlung, die SCIAMACHY messen würde. Auf Grundlage dessen wird mit Hilfe inverser mathematischer Methoden in einem iterativen Verfahren das am besten zur Messung passende Wasserdampfprofil ermittelt (Rozanov et al., 2011).

3 Ergebnisse

Was ist das Besondere an den Wasserdampfprofilen aus SCIAMACHY Messungen?
Diese Messungen sind mit wenigen Unterbrechungen von August 2002 bis April 2012 verfügbar. Das ist im Vergleich zu vielen anderen Satellitenmissionen bereits eine sehr lange, konsistente Zeitreihe. Der gesammte SCIAMACHY Datensatz umfasst ca. 4.5 Millionen horizontsondierende Messungen bei Tageslicht. Das sind über 1000 pro Tag, von denen sich nach der Filterung für Wolken etwa 700 für die Berechnung von Wasserdampf eignen. Um den gesammten Messzeitraum abzudecken, wurde zunächst nur jeder 8. Tag berechnet, 2012 dann jeder 2. Tag zwischen 45°S und 45°N. Dichtere Daten in dieser Region wurden zuerst Berechnet, da dort besonders of Profile auf Grund von Wolken herausgefiltert werden müssen. Zusätzlich wurden Messungen herausgefiltert, bei denen sich der Satellit im Bereich der Südatlantischen Anomalie (SAA) befand, dadurch kommt die

große Lücke über Südamerika zustande. Die Ergebnisse wurden dann nochmal für alle Fälle gefiltert, bei denen der Algorithmus nicht konvergiert ist.

Warum ist die Berechnung dieser Wasserdampfprofile besonders aufwendig? Um die Wasserdampfkonzentrationen bestimmen zu können muss die Mehrfachstreuung in der Atmosphäre berücksichtigt werden, dazu sind Rechnungen auf einem horizontal dichten Gitter nötig. Gleichzeitig muss ein relativ breiter Spektralbereich abgedeckt werden, um genügend Informationen über die Wasserdampfabsorbtionen zu erhalten und ein großer Datensatz bearbeitet werden. Abbildung 1 zeigt eine Zeitreihe des zonal und monatsweise gemittelten Wasserdampfes für diesen Datensatz (V3.01) für 3 verschiedene Breitenbereiche und für alle Breiten in einer Höhe von 22 km. Die Gebiete zeigen erwartungsgemäß unterschiedliche Jahresgänge und Variationen zwischen den verschiedenen Jahren.

4 Ausblick

Unser Ziel ist es, diese die Wasserdampfkonzentrationen für den gesamten Messzeitraum zu bestimmen, um mehr über den Wasserdampf in der Atmosphäre und seine Auswirkung auf das Klima lernen zu können. Deshalb arbeiten im Ramen der zweiten Phase von SHARP an der Vervollständigung von V3.01. Gleichzeitig testen wir, inwieweit die Berechnung des Wasserdampfes verbessert werden kann. Abhängig vom Ergebnis dieser Tests werden wir entscheiden, ob ein neuer, verbesserter Datensatz berechnet werden soll.

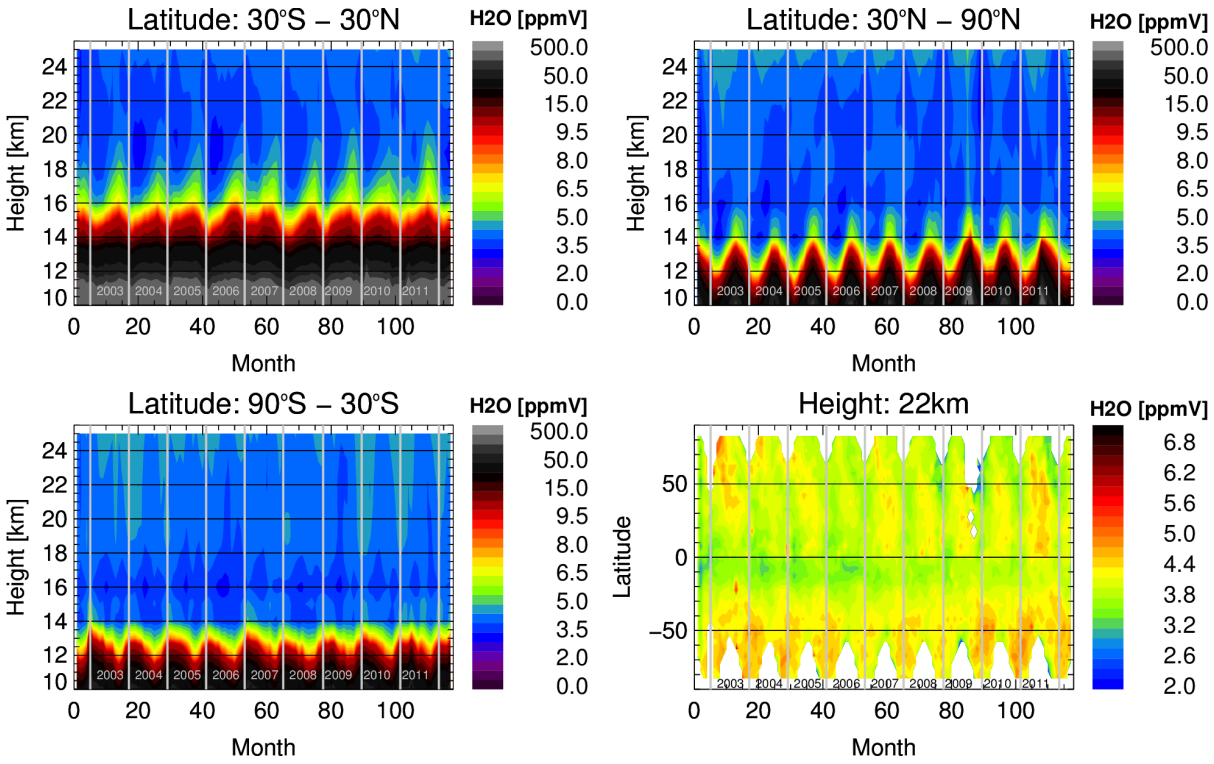

Abbildung 1: Zeitreihe des zonal und monatsweise gemitteltem SCIAMACHY Wasserdampf [ppmV] zwischen 10 und 25 km für 3 verschiedene Breitenbereiche (30°S-30°N, 30°N-90°N und 30°S-90°S und für alle Breiten auf einem 5° Gitter in 22 km Höhe, Datenversion 3.01.).

Literatur

Rozanov, A., Weigel, K., Bovensmann, H., Dhomse, S., Eichmann, K.-U.,Kivi, R., Rozanov, V., Vömel, H., Weber, M., and Burrows, J. P., Retrieval of water vapor vertical distributions in the upper troposphere and the lower stratosphere from SCIAMACHY limb measurements, Atmos. Meas. Techn., 4, 933-954, doi:10.5194/amt-4-933-2011, 2011.

Präsentationen 2012

- Weigel, K., Rozanov, A., Weber, M., Azam, F., Eichmann, S., Stiller, G. P., Bovensmann, H., and Burrows, J. P.: Status of the SCIAMACHY limb water vapor retrieval, SHARP Meeting, 03.07.2012.
- Weigel, K., Rozanov, A., Weber, Bovensmann, H., and Burrows, J. P.: Status of the limb H2O retrieval, SQWG Meeting, 21.11.2012.

Poster 2012

- Weigel, K., Rozanov, A., Azam, F., Eichmann, K.-U., Weber, M., Bovensmann, H., Stiller, G. P., and Burrows, J. P.: Water vapor in the upper troposphere and lower stratosphere from SCIAMACHY limb measurements, 2002 - 2011, EGU, Wien, 22--27. 04. 2012.
- Weigel, K., Rozanov, A., Azam, F., Eichmann, K.-U., Weber, M., Bovensmann, H., Stiller, G. P., and Burrows, J. P.: Time series of water vapor in the upper troposphere and lower stratosphere from SCIAMACHY limb measurements, Atmospheric Science Conference, Brügge, 18--22. 06. 2012

6.6 hbk00021: Understanding the Dynamics and Change in the Arctic Ocean

HLRN-Projektkennung:	hbk00021
Laufzeit:	II/2009 – II/2013
Projektleiter:	Prof. Dr. Thomas Jung
Projektbearbeiter:	W. Wang, C. Wekerle, X. Wang
Institut / Einrichtung:	Alfred-Wegener-Institute for Polar and Marine Research, Bremerhaven

Introduction

The Arctic Ocean is a very important component in the global climate system. Many processes involved in the Arctic region, for example, the sea-ice albedo feedbacks, the freshwater export into the North Atlantic, the storage and release of greenhouse gases, are key factors controlling the climate variability. The Arctic Ocean has been experiencing significant changes under global warming since the last decade. It is crucial to understand the changes in the Arctic climate dynamics and status and their impact on the climate on larger scales. In this project we use the ocean model FESOM to study a few aspects of the Arctic Ocean, including the freshwater export variability and its influence, assessing and improving the Arctic Ocean model performance, and understanding the dynamics of the Atlantic water circulation in the Arctic basins. Since the simulations use relatively large meshes and involve integrations on multi-decadal scales, our work strongly benefit from the availability of resources provided through the HLRN.

Freshwater export through CAA and the climate relevance

Due to large freshwater input (river runoff, higher precipitation than evaporation, Bering Strait inflow) the Arctic Ocean is strongly stratified with a fresh surface layer. Arctic freshwater is exported through the narrow straits of the Canadian Arctic Archipelago (CAA) and through the deep and wide Fram Strait into the North Atlantic. Freshwater exported from the Arctic Ocean could have a significant impact on the Atlantic Meridional Overturning Circulation. Therefore, an adequate representation of Arctic freshwater export in climate simulations can be crucial for the faithful hindcast and prediction of climate change and variability. The CAA straits are very narrow, so adequately resolving the CAA region in global climate models remains difficult to achieve. In this work we apply the unstructured-mesh global ocean model FESOM with mesh resolution locally refined in the CAA to study the CAA freshwater transport and its large scale relevance.

Two hindcast simulations were performed and the only configuration difference is in the horizontal mesh resolution in the CAA region. We use a nominal 1.5° horizontal resolution in the bulk of the global ocean, with it slightly refined (resolution doubled) along the coastlines. The resolution is refined to 24 km north of 50°N. This mesh is used in the reference run (LOW). The mesh in the second simulation (HIGH) has the CAA region further refined to 5 km (see Figure 1). In case LOW, the two major CAA straits are widened to allow for at least three grid points, similar to the practical approach used in traditional climate models. In the vertical the meshes have 55 z-levels with thickness of 10 m in the top 100 m and gradually

increasing downwards. Both simulations are carried out for the time period 1958-2007 and the last 40 years results are used for analysis. The CORE-II interannual atmospheric forcing dataset is used. The ocean is initialized with temperature and salinity fields from the PHC3. The sea ice is initialized with climatological fields obtained from previous simulations.

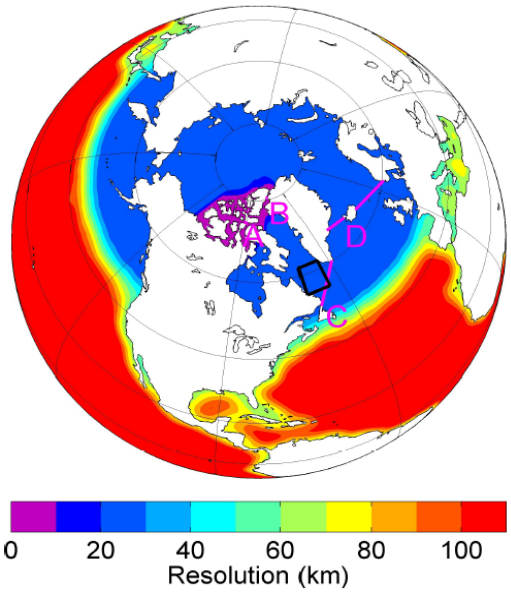

Figure 1: Northern hemisphere view of the global mesh used for experiment HIGH. The color patch shows the mesh resolution. The CAA region has a resolution of 5 km.

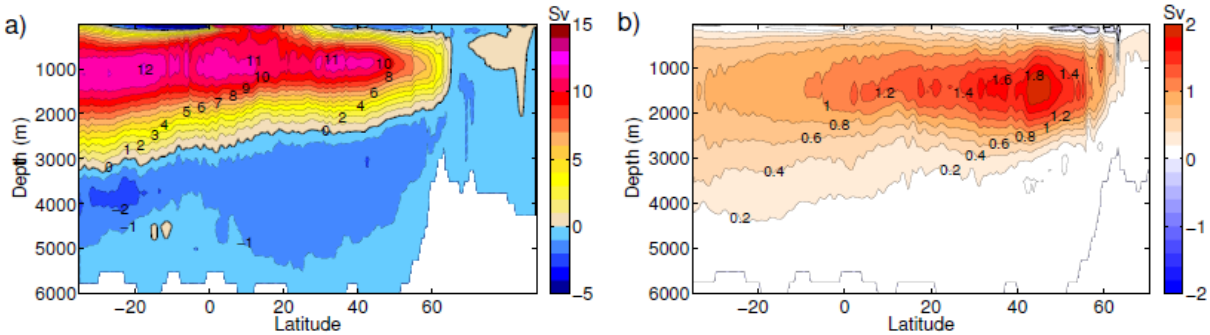

Figure 2: (a) Mean AMOC stream function for the time period 1968-2007 for experiment LOW and (b) its difference from experiment HIGH (HIGH minus LOW).

Figure 2 shows the mean Atlantic Meridional Overturning Circulation (AMOC) stream function in experiment LOW and the difference from the experiment HIGH. The strength of the intermediate overturning cell increases over the whole Atlantic when the CAA region is better resolved. The largest increment is in the North Atlantic, up to 1.98 Sv (about 27%). The pronounced change in the large-scale circulation indicates the importance of adequately resolving the CAA freshwater transport in climate simulations.

Better resolving the CAA region leads to a redistribution of Arctic Ocean freshwater exports, with more exports through the CAA and less exports through Fram Strait. This has significant effects on the stratification of the near surface waters in the Labrador Sea, thus on the convection intensity. This impact is due to the fact that freshwater from the East Greenland Current (EGC) more rigorously penetrates into the Labrador Sea interior than that from the Baffin Island Current. The total Arctic freshwater export to the North Atlantic is higher when

the CAA region is more adequately resolved. Part of the anomalous freshwater enters the Subpolar Gyre and increases the stratification south of Greenland. However, the overall ventilation and deep-water formation is intensified, leading to stronger AMOC.

Atlantic Water inflow and circulation in the Arctic Ocean

Another topic in the project is to study the dynamics of the Atlantic Water (AW) circulation in the Arctic Ocean, which has strong variability during the past decades. Numerical models quite often have difficulties in proper representation of the AW in the Arctic Ocean. We will also assess and improve the model performance in this aspect in our global simulations with regional resolution refinement.

The plan was to use different resolution in the Arctic region to simulate the AW inflow and circulation. The meshes with 24 km and 9 km resolution in the Arctic Ocean are shown in Figure 3. The configuration of the model is similar to that used in the CAA study described in section 1.1. Two passive tracers are released at Fram Strait and Barents Sea Opening to indicate the two main branches of the AW circulation. The temporal evolution of the two passive tracers in the simulation with 24 km resolution is shown in Figure 4. The AW can penetrate into the eastern Arctic basins with time, but most of the AW recirculate in the Eurasian Basins due to the confinement of bottom topography. Simulations with high resolutions in the Arctic Ocean (9 km and 3 km) will be carried out in the following year.

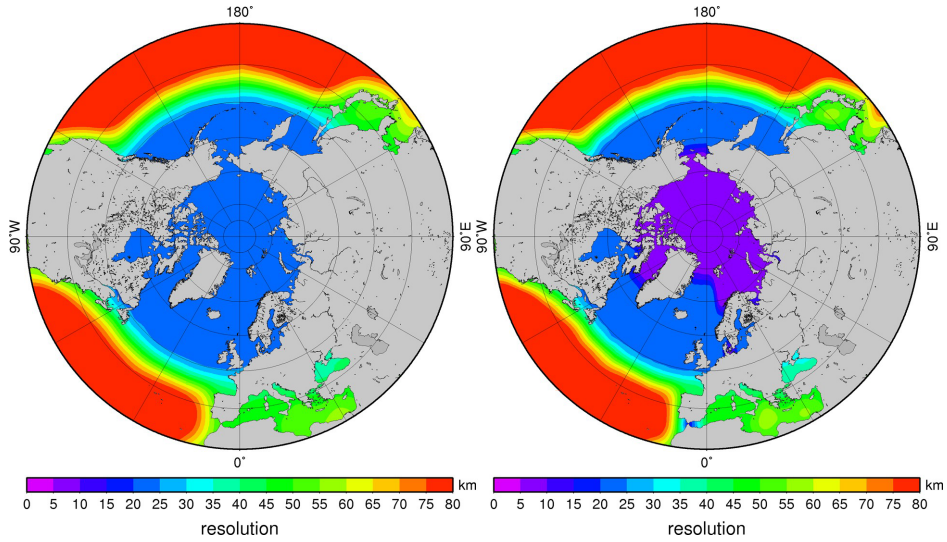

Figure 3: (left) A global mesh with 24 km resolution in the Arctic region. (right) A global mesh with 9 km resolution in the Arctic Ocean.

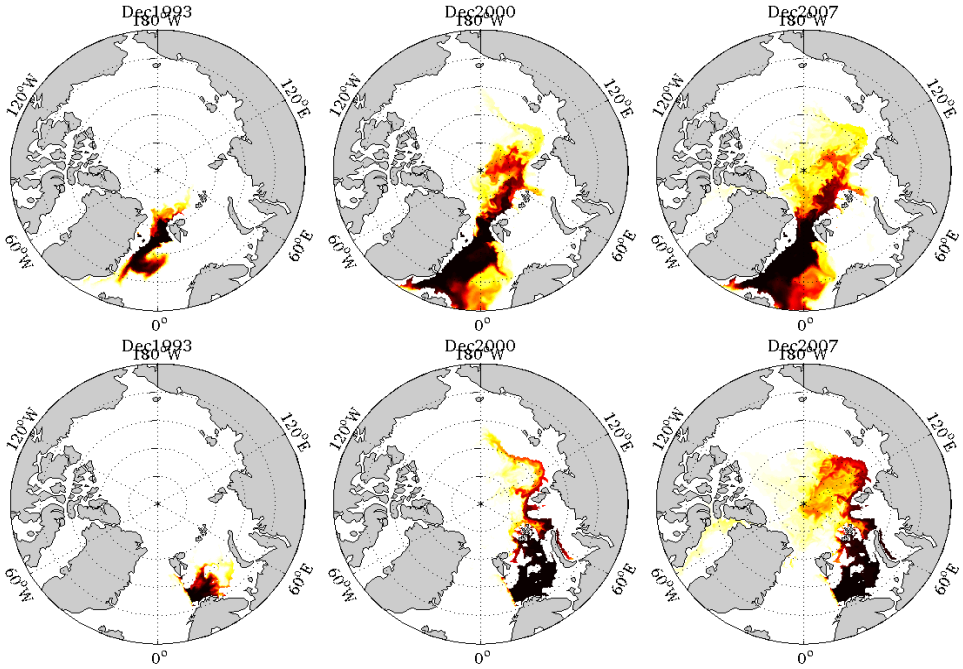

Figure 4: Temporal evolution of passive tracers released at Fram Strait (upper) and Barents Sea Opening (lower). The passive tracers indicate the two pathways of Atlantic Water circulation.

References

Wekerle C., Q. Wang, S. Danilov, T. Jung, J. Schröter and P. Myers (2013) The climate relevance of the Canadian Arctic Archipelago: A multi-resolution modeling study, GRL, submitted.

Wekerle C., Q. Wang, S. Danilov, T. Jung and J. Schröter (2013) Freshwater transport through the Canadian Arctic Archipelago in a multi-resolution global model: Model assessment and the driving mechanism of interannual variability, JGR-Oceans, submitted.

6.7 hbk00025: Die Entwicklung der tropischen Regenzone im späten Neogen

HLRN-Projektkennung:	hbk00025
Laufzeit:	II/2010 – II/2013
Projektleiter:	Prof. Dr. M. Schulz
Projektbearbeiter:	Dr. G. Jung, Dr. M. Prange
Institut / Einrichtung:	DFG-Forschungszentrum / Exzellenzcluster „Der Ozean im System Erde“ (MARUM), Universität Bremen

Kurzfassung

- In diesem Projekt werden Modellexperimente zur Abschätzung der Niederschlags- und Vegetationsentwicklung in Afrika vor 10 bis 2 Millionen Jahren durchgeführt.
- Der Schwerpunkt liegt dabei auf dem Einfluss tektonischer Faktoren wie veränderter Ozeanpassagen und der Auswirkung von Gebirgshebungen.
- Das zur Modellierung verwendete Modell ist das gekoppelte parallele Community Climate System Model (Version 3), welches Atmosphäre, Ozean, Meereis, Landoberfläche und Vegetationsbedeckung explizit berücksichtigt.
- Erste Ergebnisse zeigen einen starken Einfluss der Hebung Ost- und Südafrikas, sowie einen schwächeren, gegensätzlichen Einfluss der Hebung von Himalaya und Tibetischem Plateau auf Niederschlag und Vegetationsverteilung in Afrika.
- Ein weiterer Effekt der Hebung Afrikas ist die Verstärkung des küstennahen Auftriebs in der Benguela-Region.
- Der Einfluss der Hebung der Anden konzentriert sich sehr stark auf die südamerikanische Tropenregion.

Einleitung

Gebirgshebungsprozesse gelten, neben Öffnungen und Schließungen von Ozeanpassagen, als wichtige tektonische Prozesse, die einen nachhaltigen Einfluss auf das Klimasystem und in Folge auch auf die Vegetationsbedeckung haben (Hay, 1996). Gebirgshebungen verändern zum Beispiel die regionale Niederschlagsverteilung durch Stau- und Abschattungseffekte, haben aber auch weitreichendere Folgen für den Wärme- und Feuchtetransport in der Atmosphäre. Zudem können hohe Gebirgszüge die atmosphärische Zirkulation weltweit bis in große Höhen beeinflussen. Die topographische Hebung Ostafrikas wird als wichtiger Antriebsmechanismus für die ostafrikanische Klima- und Vegetationsentwicklung angesehen. Zudem hat diese Hebung möglicherweise einen maßgeblichen Einfluss auf den asiatischen Monsun. Die Hebung des Himalayas und des Tibetischen Plateaus und der damit verbundene Klimawandel werden häufig als Beispiel für die Verbindung von Tektonik und Klima genannt. So haben frühere Modellstudien gezeigt, dass die Hebung des Tibetischen Plateaus einen erheblichen Einfluss auf das asiatische Monsun-System hatte. Auch eine verstärkte Hebung der Anden wirkt sich nicht nur auf das

Klima Südamerikas aus. Nachdem die Anden das einzige Hindernis der Strömung auf der Südhalbkugel sind, nimmt man an, dass sie den globalen Wärme- und Feuchtetransport stark beeinflussen. Ähnlich globale Auswirkungen werden für die Hebung der Rocky Mountains und des Colorado Plateaus vermutet.

Um die verschiedenen Einflussfaktoren sowie mögliche Rückkopplungsmechanismen im Klimasystem im Zeitraum des späten Miozäns und des Pliozäns (vor ca. 10-2 Millionen Jahren) abzuschätzen, werden verschiedene Sensitivitätsläufe mit Hilfe eines globalen, gekoppelten Klimamodells durchgeführt. Es wird das parallele *Community Climate System Model* (Version 3) verwendet. Dieses Modell simuliert in gekoppelten Teilmodellen Atmosphäre, Ozean, Meereis und Landoberflächenprozesse inklusive der Vegetations-bedeckung.

Ergebnisse

Im Folgenden werden einige Ergebnisse der Sensitivitätsexperimente mit verringerter Topographie der folgenden Regionen dargestellt:

- Anden
- Rocky Mountains/Colorado Plateau
- Himalaya/Tibet Plateau
- Ost-/Südafrika

Es zeigt sich, dass die Hebung von sowohl Ost- und Südafrika als auch des Himalayas und des Tibetischen Plateaus die Afrikanisch-Asiatische Monsunzirkulation beeinflussen.

Die Erhöhung des Tibetischen Plateaus sowie des Himalayas bewirkt erwartungsgemäß eine Verstärkung des asiatischen Monsuns. Daneben zeigt sich dabei auch eine Abnahme der Niederschlagsmengen über Zentralafrika sowie eine Zunahme über Ostafrika.

Die Hebung Ost- und Südafrikas hat einen starken Einfluss auf das Niederschlagsgeschehen (Abbildung 1) Afrikas. Die Erhöhung der Topographie führt zu einer Verstärkung der äquatorialen Passatwinde über dem tropischen Atlantik, was dort zu einer höheren Verdunstung und einer Zunahme des Feuchtetransportes mit dem Sommermonsun nach Zentralafrika führt. Dies wiederum bewirkt dort eine Intensivierung des Niederschlags, ein Effekt, der durch den Staueffekt der ostafrikanischen Berge noch verstärkt wird. Über Ostafrika kann hingegen, in Übereinstimmung mit den Ergebnissen von Sepulchre et al. (2006), eine Abnahme der Niederschläge beobachtet werden.

Ein weiterer bedeutsamer Effekt der Hebung Afrikas ist eine damit verbundene Verstärkung des küstennahen Auftriebs vor Südwest-Afrika, der zu einer signifikanten Verringerung der oberflächennahen Meerestemperatur in dieser Gegend führt (Abbildung 2). Grund hierfür ist unter Anderem der Kanalisierungseffekt der küstennahen Strömung durch die steile Küstentopographie, die zu einer Verstärkung des Benguela-Jets führen. Dieses bodennahe Starkwindband ist ein maßgeblicher Antrieb für den küstennahen Auftrieb und über positive Rückkopplungsmechanismen mit diesem gekoppelt (Nicholson, 2010).

Aufgrund der Hebung der Anden zeigt sich für Südamerika eine deutliche Zunahme der Niederschläge in den Zentralanden bedingt durch die Zunahme des Feuchtetransports mit dem südamerikanischen Low-Level Jet, sowie die Stauwirkung des Gebirges, vergleichbar mit den Ergebnissen von Poulsen et al. (2010). In den nördlichen Anden zeigt sich eine starke Niederschlagsreduktion in weiten Teilen des Amazonas-Einzugsgebiets (Abbildung 3).

Die Hebung der Anden sowie auch die Hebung der Rocky Mountains und des Colorado Plateau wirken sich in erster Linie auf den süd- (Anden) bzw. nord- (Rocky Mountains) - amerikanischen Kontinent aus und zeigen eine geringere Fernwirkung als erwartet.

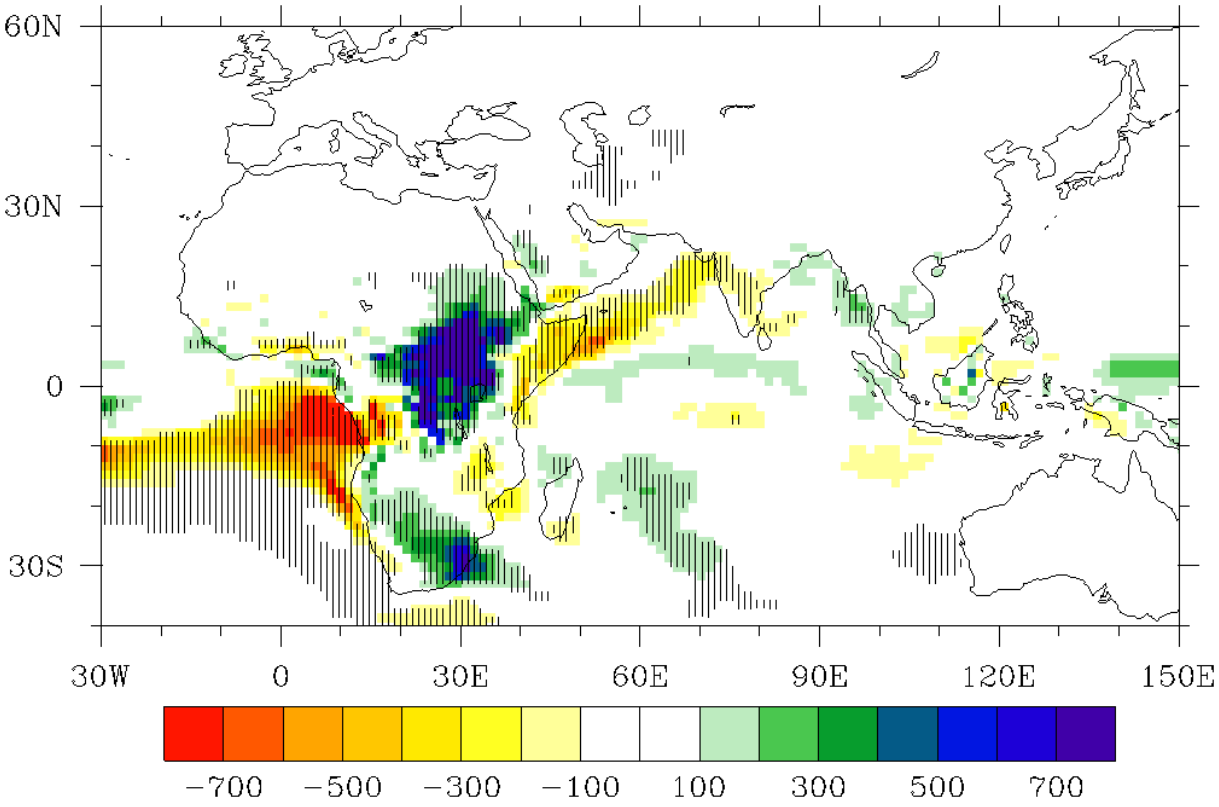

Abbildung 1: Effekt der Hebung von Süd-/Ostafrika auf den mittleren Jahresniederschlag [mm] (Mittel über 100 Jahre), gestrichelt: signifikante Werte (Signifikanzniveau: 0.1%).

References:

(1) Hay, W.W. (1996): Tectonics and Climate, *Geol. Rundsch*., V.85, S. 409-437

(2) Sepulchre, P., G. Ramstein, F. Fluteau, M. Schuster, J.-J. Tiercelin and M. Brunet (2006): Tectonic Uplift and Eastern Africa Aridification, *Science*, Vol. 313 no. 5792 pp. 1419-1423,DOI: 10.1126/science.1129158

(3) Nicholson, S. E. (2010): A low-level jet along the Benguela coast, an integral part of the Benguela current ecosystem. *Climatic change*, *99*(3-4), 613-624.

(4) Poulsen, C. J., Ehlers, T. A., and Insel, N. (2010): Onset of convective rainfall during gradual late Miocene rise of the central Andes. *Science*, *328*(5977), 490-493.

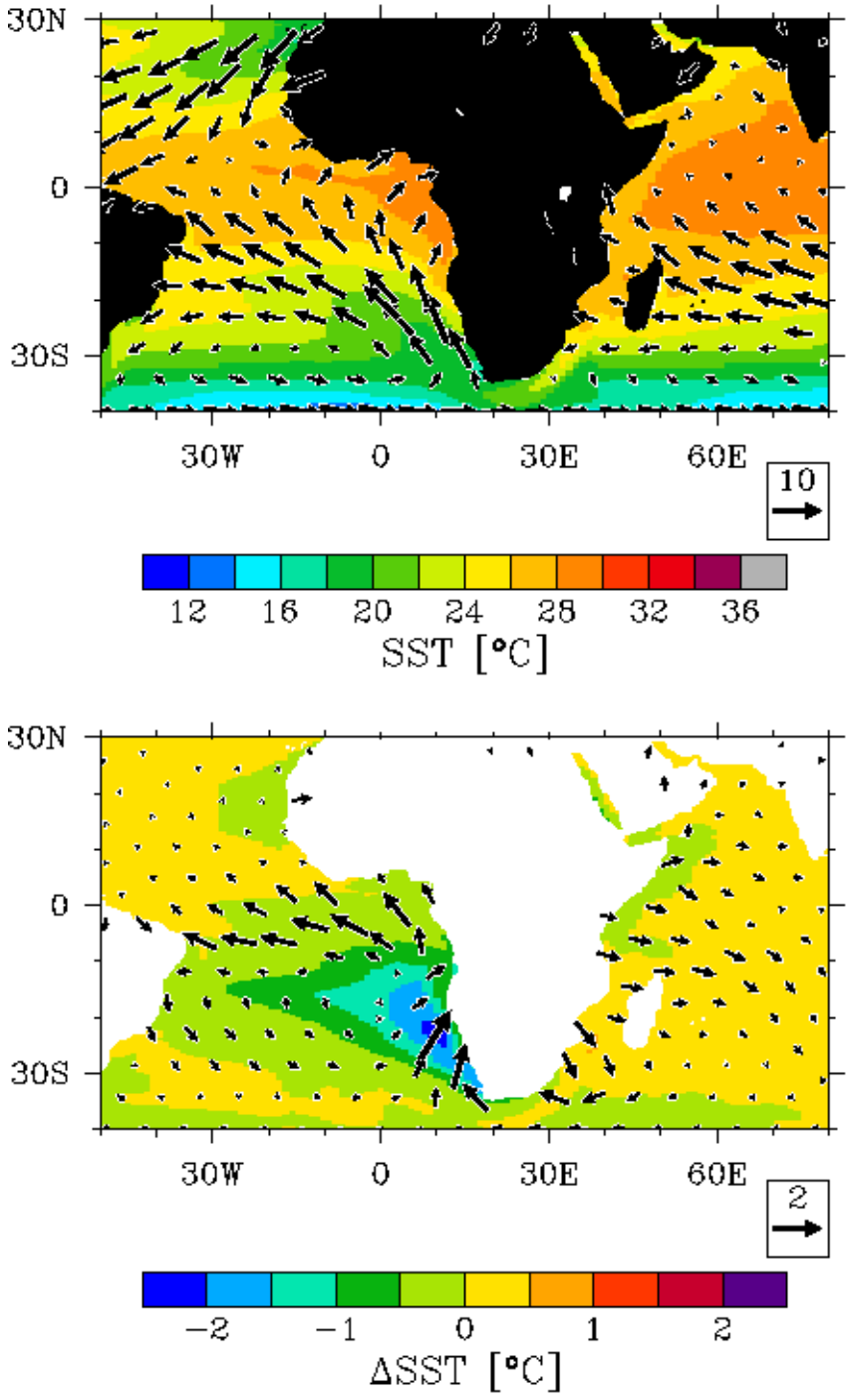

Abbildung 2: Meeresoberflächentemperatur (SST) [°C] und horizontaler Wind [m/s] für heutige Topographie (oben) und die Änderungssignale aufgrund der Gebirgshebung Süd- und Ostafrikas (unten).

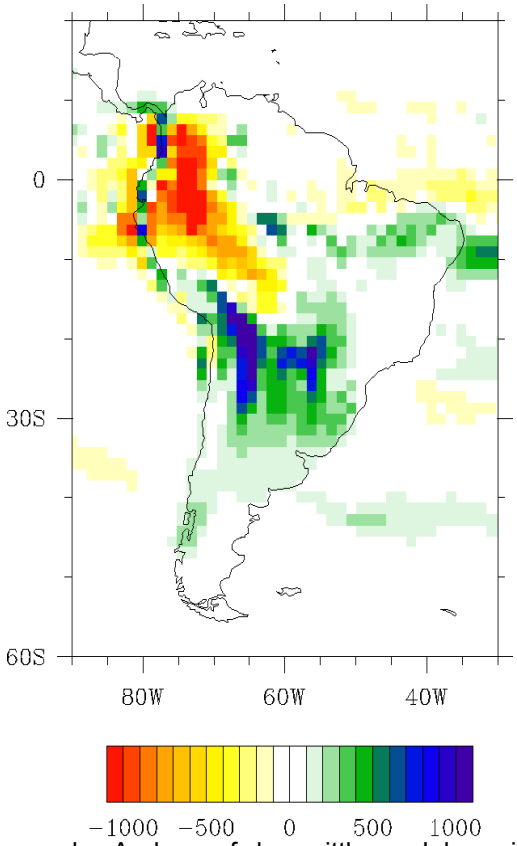

Abbildung 3: Effekt der Hebung der Anden auf den mittleren Jahresniederschlag [mm] (Mittel über 100 Jahre).

Poster Presentations:

(1) Simulating mountain uplift and African climate and vegetation evolution in the late Neogene, (2012, Jung, Prange, Schulz), 3rd International Conference on Earth System Modelling, Hamburg, Germany

(2) Modeling the impact of mountain lifting in the late Neogene on the African-Asian Monsoon circulation and African vegetation development, (2010, Jung, Prange, Schulz), PAGES 2nd Global Monsoon Symposium, Shanghai, China.

Oral Presentation:

Jung, G.; Prange, M.; Schulz, M. (2012): Mountain uplift and the evolution of the African rainbelt in the late Neogene, EGU General Assembly, Vienna, Austria.

Publications:

Jung, G.; Prange, M.; Schulz, M. (in preparation): Neogene intensification of the Benguela Upwelling System due to African uplift.

6.8 hbk00027: Wie stabil ist das ozeanische Förderband? Atmosphärische Feuchtetransporte und thermohaline Zirkulation: Untersuchung möglicher Rückkopplungsmechanismen für abrupte Klimaschwankungen

HLRN-Projektkennung:	hbk00027
Laufzeit:	III/2010 – III/2013
Projektleiter:	Prof. Dr. Michael Schulz
Projektbearbeiter:	Huadong Liu, Dr. Matthias Prange
Institut / Einrichtung:	Fachbereich Geowissenschaften und Zentrum für Marine Umweltwissenschaften (MARUM), Universität Bremen

Übersicht

- Der Export von Wasserdampf aus dem tropischen Atlantik in den Pazifik über Nordostpassate spielt eine maßgebliche Rolle für die Aufrechterhaltung der nordatlantischen Tiefenwasserbildung und somit der globalen Ozeanzirkulation. Änderungen in diesem Feuchtetransport können daher einen wichtigen Rückkopplungsmechanismus für abrupte Klimaschwankungen darstellen.
- In diesem Projekt wird die räumlich hochaufgelöste Version eines komplexen Klimamodells verwendet, um die Variabilität tropischer Wasserdampftransporte während der letzten 20 000 Jahre zu untersuchen.
- Die Modellsimulationen sollen Aufschluss darüber geben, wie sich Änderungen der Ozeanzirkulation auf den tropischen Wasserkreislauf auswirken und ob Feuchtetransportänderungen einen positiven oder negativen Rückkopplungsmechanismus für Klimaschwankungen darstellen.
- Das zur Modellierung verwendete Modell ist das gekoppelte parallele Community Climate System Model (Version 3), welches Atmosphäre, Ozean, Meereis und Landoberfläche simuliert.

The tropical eastern Pacific is a key area for monitoring climate variability, as it is highly sensitive to ITCZ (Intertropical Convergence Zone) and ENSO (El Niño-Southern Oscillation) dynamics. Atmospheric water-vapor transport from the Atlantic to the Pacific across Central America plays an important role in maintaining high Atlantic sea-surface salinities and hence may exert a strong control on the strength and stability of the Atlantic thermohaline circulation (THC; e.g., Broecker et al., 1990; Stocker and Wright, 1991; Zaucker et al., 1994; Schmittner et al., 2000; Hasumi, 2002). Whether variations in the Atlantic-to-Pacific vapor transport acted as a positive or negative feedback on thermohaline circulation changes during Heinrich Stadial 1, however, is unclear as previous results from paleosalinity reconstructions and model experiments lead to different conclusions (Prange et al., 2010). A sequence of new sediment cores from high deposition rate locations along the Colombian and Panamanian margins provides an opportunity to improve our understanding of the role of the tropical hydrological cycle as a potential driving force for global climate change (Benway et al., 2006; Leduc et al., 2007). Simulations of Holocene and deglacial climate states, using a high-resolution version of the comprehensive climate model CCSM3, will help to interpret the proxy records and to set them into a global dynamical context. In particular, the model will provide quantitative information about changes in the Atlantic-to-Pacific water vapor flux,

while the proxy records will be indispensable for verifying the model output.

First, a 900-year long simulation for the late Holocene with pre-industrial boundary conditions (PI run hereafter) has been carried out as control run. This experiment forms the basis for a freshwater hosing experiment (PI_fre hereafter) in order to simulate the influence of THC slowdowns on the eastern tropical Pacific hydroclimatology under pre-industrial boundary conditions. In the hosing experiment, 0.2 Sv (1 Sv = 10^6 m^3/s) of freshwater was injected into the northern North Atlantic for 400 years. As a result, Atlantic meridional overturning decreased by approximately 50% compared to the control run, leading to a substantial cooling in the Northern Hemisphere.

Second, a 600-year long simulation for the early Holocene (EH hereafter) has been performed with the orbital forcing and greenhouse gas concentrations of 8.5 ka before present. Then, a freshwater hosing experiment with the same boundary conditions (EH_fre hereafter) has been carried out, also with 0.2 Sv of freshwater discharge into the northern North Atlantic for 400 years.

Third, a simulation for the Last Glacial Maximum (LGM hereafter) has been performed for 600 years under LGM boundary conditions. Then, a freshwater hosing experiment with the LGM boundary conditions (LGM_fre hereafter) has been carried out for 400 years, introducing an anomalous freshwater flux of 0.2 Sv into the northern North Atlantic as surrogate for Heinrich Stadial 1.

The annual mean moisture transports from the Atlantic to the Pacific in the above mentioned simulations were computed based on daily model output (Table 1). Compared to the PI run, the moisture transport in the LGM run decreases by 16%. An increase of northeasterly trades is overcompensated by lower atmospheric moisture content. The net moisture transports across Central America in the experiments PI, EH and LGM show no difference comparing to their freshwater hosing experiments. Induced by the slowdown of the Atlantic thermohaline circulation, strengethened trade winds favor enhanced cross-isthmus moisture transport from the Atlantic to the Pacific. However, in absolute terms, this enhanced flux is compensated by lower atmospheric moisture content of the cooler air.

Table 1. Net moisture transport across Central America (here along the 6°N-14°N segment computed with 20 year daily model output).

Experiment	PI	PI_fre	EH	EH_fre	LGM	LGM_fre
Net moisture transport (Sv)	0.31	0.31	0.28	0.28	0.26	0.26

Fig. 1a shows the difference in P–E between the experiments LGM and LGM_fre in the annual mean. The dipole structure of the P-E difference in the LGM is similar to the late Holocene (Fig. 1b) in our simulation. This finding suggests that the appearance of the dipole structure is a robust feature, independent of the orbital forcing. The P–E pattern in the Panama Bight region exhibits a dipole structure with wetter conditions in western Colombia and dryer conditions over the Gulf of Panama and west of Costa Rica. This dipole pattern during Heinrich Stadial 1 is consistent with some published sea-surface paleosalinity reconstructions of the last termination. Our model results would help to reconcile the conflicting proxy evidence. We conclude that the cross-isthmus vapor flux feedback on thermohaline circulation variations was negligible during Heinrich Stadial 1.

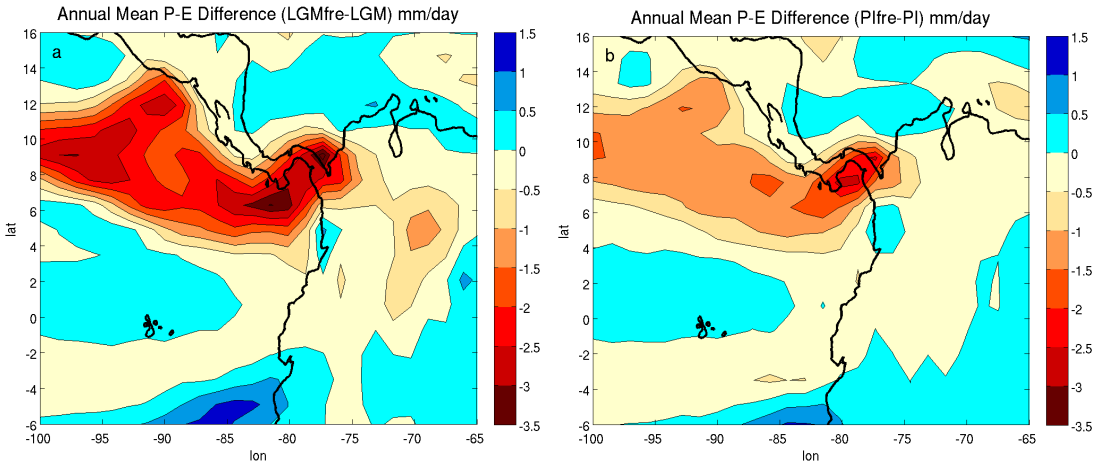

Figure 1. a) Annual mean P-E difference between the experiments LGM_fre and LGM. b) Annual mean P-E difference between PI_fre and PI. The last 100 years of each run have been used for averaging.

References:

Benway, H. M., A. C. Mix, B. A. Haley, and G. P. Klinkhammer (2006), Eastern Pacific Warm Pool paleosalinity and climate variability: 0–30 kyr, Paleoceanography, 21, PA3008, doi:10.1029/2005PA001208.

Broecker, W. et al. (1990), A salt oscillator in the glacial Atlantic?, Paleoceanography, 5, 469–477.

Hasumi, H. (2002), Sensitivity of the Global Thermohaline Circulation to Interbasin Freshwater

Leduc, G. et al. (2007), Moisture transport across Central America as a positive feedback on abrupt climate changes, Nature, 445, 908–911, doi:10.1038/nature05578.

Pahnke, K. et al. (2007), Eastern tropical Pacific hydrologic changes during the past 27,000 years from D/H ratios in alkenones, Paleoceanography, 22, PA4214, doi:10.1029/2007PA001468.

Prange, M., S. Steph, M. Schulz and L.D. Keigwin (2010), Inferring moisture transport across Central America: Canmodern analogs of climate variability help reconcile paleosalinity records? Quat. Sci. Rev., 29, 1317–1321.

Schmittner, A., C. Appenzeller, and T. F. Stocker (2000), Enhanced Atlantic freshwater export during El Niño, Geophys. Res. Lett., 27,1163–1166.

Stocker, T. F., and D. G. Wright (1991), Rapid transitions of the ocean's deep circulation induced by changes in surface water fluxes, Nature, 351, 729–732.

Zaucker, F., T. F. Stocker, and W. S. Broecker (1994), Atmospheric freshwater fluxes and their effect on the global thermohaline circulation, J. Geophys. Res., 99, 12, 443–12, 457.

Poster:

Liu, H.; Prange, M.; Schulz, M. (2013): Hydroclimatologic variations in the eastern tropical Pacific during Heinrich Stadial 1, EGU General Assembly, Vienna, Austria.

Förderung: DFG, Schwerpunktprogramm 1266 (Interdynamik)

6.9 hbk00030: Sea surface topography and mass transport of the Antarctic circumpolar current

HLRN-Projektkennung:	hbk00030
Laufzeit:	IV/2011 – III/2013
Projektleiter:	Prof. Dr. Thomas Jung[1,2]
Projektbearbeiter:	L. Nerger[1], J. Schröter[1], F. Kauker[1,3], R. Schnur[1,3], A. Androsov[1]
Institut / Einrichtung:	[1] Alfred-Wegener-Institute for Polar and Marine Research, Bremerhaven [2] University of Bremen [3] O.A.Sys GmbH, Hamburg

Introduction

This compute project is related to the DFG-funded project “GEOTOP 3”. The main objective is the determination of the absolute, but temporally changing ocean circulation flow field, and of associated mass and heat transports. The focus is on the Atlantic sector of the Antarctic Circumpolar Current (ACC). A particular focus is on the Weddell Sea, which is one of the most dynamic ocean areas and one of the most critical regions for global climate. The project requires extended runs of a state-of-the-art ocean circulation model including the assimilation of dynamic ocean topography (DOT) derived from satellite altimetry combined with gravimetry and oceanographic in-situ data. The Finite Element Sea-ice Ocean Model (FESOM) with unstructured meshes is used with a global mesh and locally refined resolution in the Atlantic section of the Southern Ocean. The assimilation is performed using ensemble-based methods provided by the Parallel Data Assimilation Framework (PDAF), which makes excellent use of supercomputers. As a large number of processors is required for the assimilation, the project does strongly benefit from the resources provided by HLRN.

Methodology

This project uses the Finite Element Sea-ice Ocean Model FESOM that solves the hydrostatic ocean primitive equations using the finite element method. FESOM uses unstructured triangular meshed and simulated both the ocean and sea ice on the same unstructured triangular 2D mesh. Regional processes can be simulated with increased local resolution without traditional nesting.

Previous work in this project was performed with the model of constant resolution and without a dynamical oce-ice component (Janjic et al. 2012a,b). Following recent developments in data assimilation algorithms, we will apply the Error Subspace Transform Kalman Filter (ESTKF, Nerger et al. 2012) with localization for the assimilation. In addition, a smoother extension is used, which transports the observational information also backward in time. The algorithms are implemented within the Parallel Data Assimilation Framework (PDAF, Nerger and Hiller 2013). In the analysis step of the ESTKF the full model state, consisting of temperature, salinity, sea surface height (SSH), and velocity fields is updated. The fields describing the sea-ice are not modified during the analysis step of the assimilation system.

Assimilation Results

During this project year, the smoother methodology has been assessed using experiments with synthetic observations. A large number of experiments, each over one year of simulation time, was performed. These experiments served to adjust data assimilation parameters.

Next to the experiments with synthetic observations, the real DOT data was assimilated. The experiments show a significant reduction of the deviation of the model state from the observations by the data assimilation. Here, the smoother can reduce the deviation even more than the filter of the ESTKF. Figure 1 shows the root mean square (RMS) deviations from the 10-day forecasts during an assimilation experiment. Combined with the RMS deviations of the filter analysis, a saw-tooth curve is visible that shows to which extent the filter analysis reduces the RMS deviation of each forecast. The RMS deviations from the smoother show smaller deviations with the largest reduction close to the beginning of the experiments.

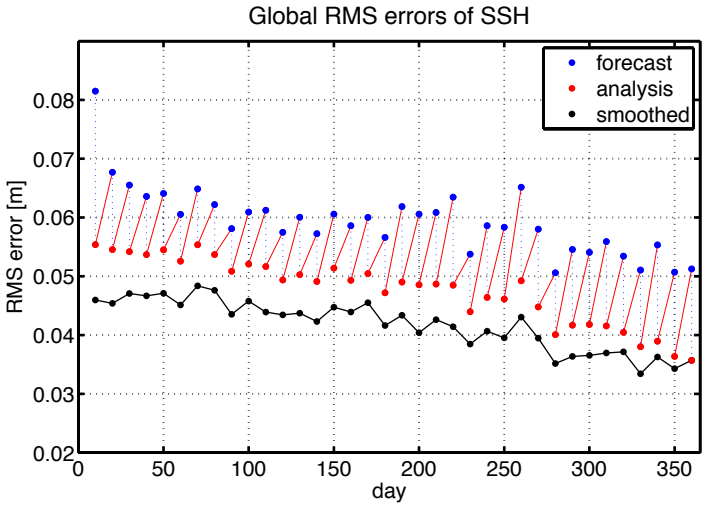

Figure 1: Root mean square differences between the model state and the observations.

Maps of the deviations between the estimated model state and the observations averaged over the one-year experiment are displayed in Figure 2. The left side shows the deviations for the filter analysis while the right hand side shows the deviations for the smoother. The smoother reduces the deviations significantly. However, there are still regions with larger deviations up to about 0.25m. These are caused by biases in the model forecasts. During the next project year, the focus will be on reducing these biases in order to improve the state estimates obtained with the data assimilation technology.

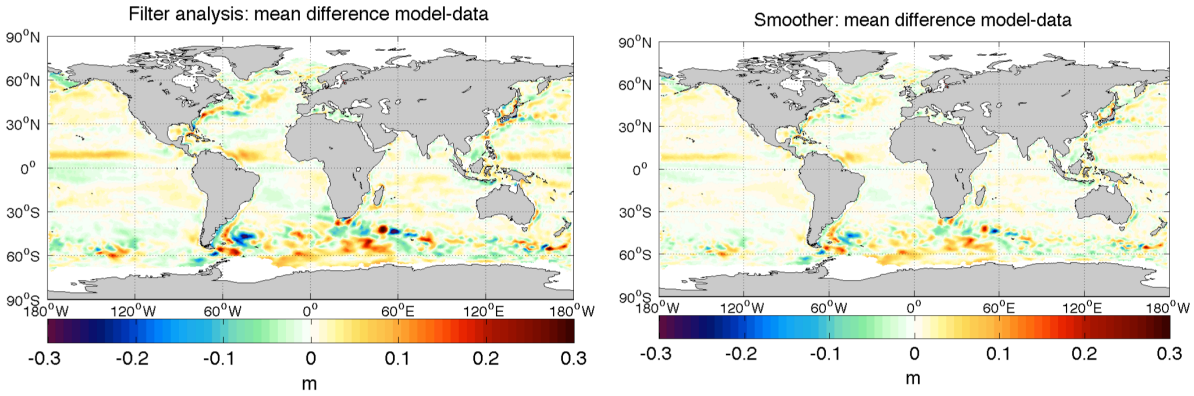

Figure 2: Annual mean difference between the model state and the observations. (left) Difference for the filter analysis; (right) difference for the smoother estimates.

References

Janjic, T., J. Schröter, A. Albertella, W. Bosch, R. Rummel, R. Savcenko, J. Schwabe, and M. Scheinert, 2012a: Assimilation of geodetic dynamic ocean topography using ensemble based Kalman filter. J. of Geodynamics **49**, 92-98

Janjic, T., J. Schröter, R. Savcenko, W. Bosch, A. Albertella, R. Rummel, and O. Klatt, 2012b: Impact of combining GRACE and GOCE gravity data on ocean circulation estimates. Ocean Sci. **8**, 65-79.

Nerger, L., T. Janjic, J. Schröter, and W. Hiller, 2012: A unification of ensemble square-root filters. Mon. Wea. Rev. **140**, 2335-2345.

Nerger, L., and W. Hiller, 2013: Software for Ensemble-based Data Assimilation Systems - Implementation Strategies and Scalability. Computers and Geosciences. **55**, 110-118

6.10 hbk00032: **Climate change and atmosphere/ocean interaction in the coupled FESOM/ECHAM model**

HLRN-Projektkennung:	hbk00032
Laufzeit:	II/2012 – I/2013
Projektleiter:	Prof. Dr. Thomas Jung[1,2]
Projektbearbeiter:	Dmitry Sidorenko[2], Thomas Rackow[2], Tido Semmler[2], Qiang Wang[2], Xuezhu Wang[2], Sergey Danilov[2], Jens Schröter[2], Claudia Wekerle[2]
Institut / Einrichtung:	[1] also at University of Bremen [2] Alfred-Wegener-Institute for Polar and Marine Research, Bremerhaven

Abstract

In this project we evaluate a newly established coupled climate model for representing the mean climate and variability. The coupled model consists of the Finite-Element Sea-Ice Ocean Model (FESOM) and the atmospheric model ECHAM6. The major difference of this setup to other climate models is the ocean component which supports variable resolution allowing to refine the areas of particular interest such as the North Atlantic, the tropics, the coastlines or narrow straits. Our intention is to exploit the new setup in order to improve the climate simulations by increasing the resolution in the key regions of the climate system. The current computations have been performed on multi-decadal time scales, using different spatial resolutions in the tropical region. Extensions of these simulations as well as sensitivity experiments on the Arctic sea-ice extent are planned for the second quarter of 2013.

1. Coupled model setup

The ***ocean-sea ice*** component (FESOM) has been already described and validated in numerous works as a standalone ocean-sea ice model (see eg. Danilov et al., 2004; Wang et al., 2008; Timmermann et al., 2009, Sidorenko et al., 2011). Two FESOM configurations differing by the surface meshes are used in this work. The first mesh (further referred to as **ref**) is shown in figure 1 (left panel) and has a nominal resolution of 120km and about 20km in the Arctic. The second mesh (further referred to as **tropics**) is shown in figure 1 (right panel) and is identical to the **ref** mesh except for the equatorial belt, where the resolution gradually increases to 20km.

The ***atmosphere*** is simulated by the 6th generation of the ECHAM general circulation model (ECHAM6), developed by the Max Planck Institute for Meteorology. We use T63L47 configuration and the prescribed greenhouse gas concentration from 1990.

The ***coupling technique*** follows the standard practice where moisture and heat fluxes are computed in the atmospheric part. The technical complexity of this setup is linked to an exchange between unstructured and structured meshes. These have different geometry, representation of coastlines and different rules for the flux definition. Additional strategies have been developed in order to preserve the flux conservation. Coupling itself has been achieved via the parallel OASIS3MCT coupler and additional exploitation of a regular exchange mesh. The latter has been introduced in the ocean part.

2. Model simulations

The system was run with **ref** and **tropics** meshes used for FESOM and T63L47 configuration for ECHAM6. Two runs have been performed for each configuration differing by the initial conditions. In the **cold start** we initialize FESOM with the Polar Science Center Hydrographic Climatology (PHC) [Steele et al. 2001] and ECHAM6 with the default initial restart. In the **spin up** simulations we initialize FESOM with the ocean state after a 60 year ocean-only FESOM simulation driven by the CORE2 Global Air-Sea Flux Dataset [Large and Yeager, 2008] and ECHAM6 with the output from the cold start after 5 years. The reason to perform both the cold start and the spin up simulations is that we want to explore if there are systematic differences between the two initialization techniques and if one method is preferable over the other for future experiments. The existing model simulations and the available years are summarized in the table below.

mesh/initialization	**cold start**	**spin up**
ref	300	200
tropics	110	120

Table1: years of integration available for each run

3. Technical achievements

1. The atmospheric component ECHAM5 in the old setup is replaced by ECHAM6. ECHAM6 became available in December 2012 and has some physical advantages against older versions.
2. The parallel OASIS4 coupler has been replaced by OASIS3 MCT in order to improve overall performance of the coupled system.

4. Some model results

Existing simulations have been analyzed for differences between model results and observations, long term trends and variability. The sea surface temperature and salinity biases mainly resemble those from state-of-the art coupled climate models with comparable resolution. One of the issues is the lack of stratocumulus clouds in the subtropical South Pacific and South Atlantic leading to too much absorption of shortwave radiation by the ocean in these areas. Furthermore, freshening and cooling of the Labrador Sea is a well-known problem [*see eg., Scaife et al., 2011, Jochum et al., 2008, Stouffer et al., 2006]* leading to decreased mixed layer depth and suppression of deep water production. These anomalies leave some imprint on the meridional overturning streamfunction (MOC) and its variability. In figure 2 the mean MOC (left panel) and the time series of its maximum at 45N in all simulations are shown. The time series indicate that the model memory for the initial condition is ca. 50 years and the simulations are similar in terms of variability behavior afterwards. The time series of the Drake Passage transport supports this hypothesis. However, since the climate system also exhibits variability on a time scale of 100 years an extension of these simulations is needed. We plan to use the results to publish two papers describing the new model system, its long-term climatology as well as its variability on different time scales.

5. Ongoing activities

The current activities in the group enclose four different scopes:

1. Comparison of performance of the FESOM/ECHAM6 to the other existing climate models
2. El Niño-Southern Oscillation (ENSO) and North Atlantic oscillation (NAO) and the influence of tropical resolution
3. Developing strategies for improving the sub-Arctic cold bias by means of increasing resolution over Northern North Atlantic. The improved setting will be further used to compute Greenland Ice Sheet (GIS) melting scenarios.
4. Sensitivity experiments on the response of the climate system to vanishing Arctic sea-ice. Simulations branching off from one of the existing simulations (dependent on the over-all performance for current climate conditions) with reduced sea-ice cover are planned.

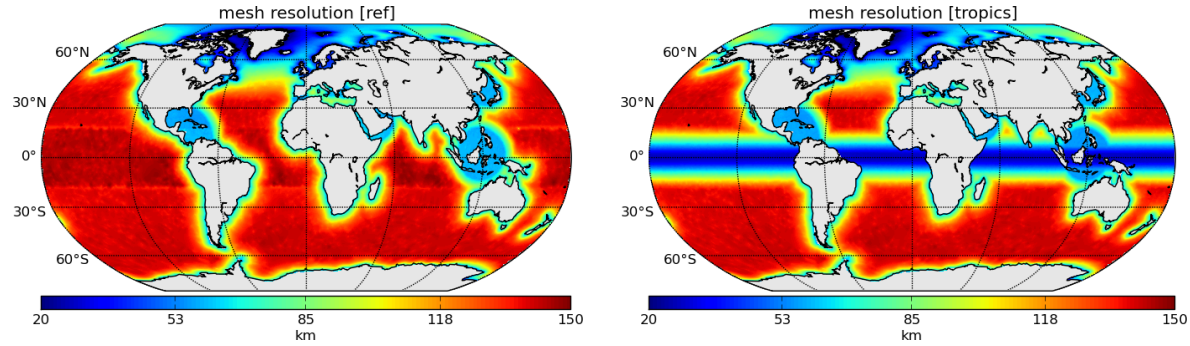

Figure 1: resolutions for the **reference** mesh (left panel) and the **tropics** mesh (right panel)

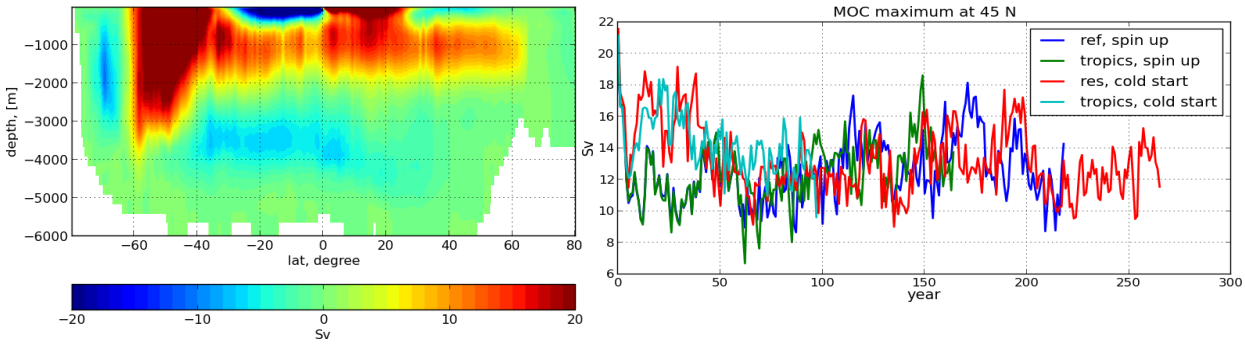

Figure 2: global meridional overturning streamfunction, mean over last 20 years from the ref/cold start simulation (left panel) and the time series of it's maximum at 45°N for all simulations (right panel) are shown.

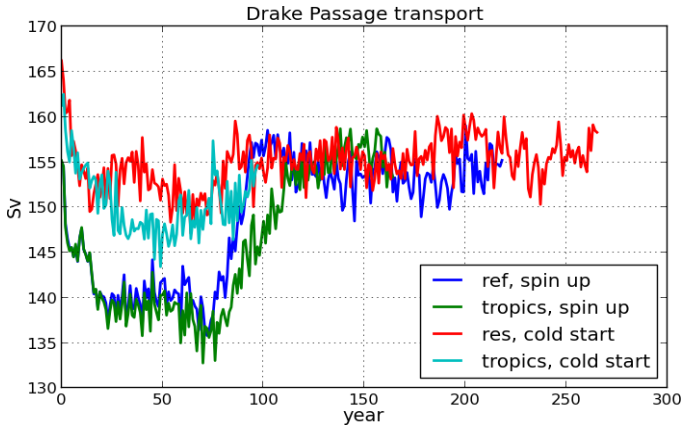

Figure 3: time series of the transport across the Drake Passage for all simulations.

References

Danilov S., G. Kivman, and J. Schröter (2004), *A finite-element ocean model: principles and evaluation,* Ocean Modell., 6(2):125–150

Jochum, M., G. Danabasoglu, M. Holland, Y.-O. Kwon, and W. G. Large (2008), Ocean viscosity and climate, J. Geophys. Res., 113, C06017, doi:10.1029/2007JC004515

Scaife, A. A., D. Copsey, C. Gordon, C. Harris, T. Hinton, S. Keeley, A. O'Neill, M. Roberts, and K. Williams (2011), Improved Atlantic winter blocking in a climate model, Geophys. Res. Lett., 38, L23703, doi:10.1029/2011GL049573

Sidorenko, D., Wang, Q., Danilov, S., Schröter, J., (2011). *FESOM under Coordinated Ocean-ice Reference Experiment forcing.* submitted to Ocean Dynamics

Steele, M., R. Morley, and W. Ermold, 2001: PHC: A global ocean hydrography with a high-quality Arctic Ocean. *J. Climate*, 14, 2079–2087

Stouffer, R J; Broccoli, A J; Delworth, T L; Dixon, K W; Et al. (2006) "GFDL's CM2 Global Coupled Climate Models. Part IV: Idealized Climate Response." Journal of Climate. American Meteorological Society

Timmermann R., S. Danilov, J. Schröter, C. Böning, D. Sidorenko, and K. Rollenhagen (2009), *Ocean circulation and sea ice distribution in a finite element global sea ice-ocean model*, Ocean Modell., 27 (3-4), 114-129.

Wang Q., S. Danilov, and J. Schröter (2008), *Finite element ocean circulation model based on triangular prismatic elements, with application in studying the effect of topography representation,* J. Geophys Res., 113, C05015, doi:10.1029/2007JC004482.

6.11 hbp00003: Encounters of Neutron Stars

HLRN-Projektkennung:	hbp00003
Laufzeit:	IV/2010 – III/2012
Projektleiter:	Prof. Dr. C. Lämmerzahl[1], Prof. Dr. S. Rosswog[2]
Projektbearbeiter:	C. Lämmerzahl, S. Rosswog
Institut / Einrichtung:	1: Universität Bremen 2: Jacobs University Bremen

1. Overview

- Mergers of two compact objects (either two neutron stars or a neutron star and a black hole) are the prime targets of existing gravitational wave detectors
- The first direct gravitational wave detections will likely be marginal, therefore it is of paramount importance to understand which additional signals that go along with such an encounter. Such signals will enhance the effective detector sensitivity and allow to place mergers in their astrophysical context (host galaxy, surrounding gas etc.)
- Our calculations predict two types of electromagnetic signals:
  a) A transient signal ("Macronova") that is powered by radioactive decays occuring within the ejected material from such a compact encounter.
  b) The ejecta are shot into the surrounding galaxy with ~ 10 %of the speed of light. When they are braked by the surrounding gas they produce a detectable signal at radio wavelengths that is visible for years.
- We have calculated the distribution of the heavy elements that are forged in such an event and they turn out to closely reproduce the observed abundance distributions of the heaviest elements in the cosmos (among them gold and platinum) making such mergers the prime candidates for the cauldrons of these elements.

2. Introduction

Stars with more than eight solar masses end their lives in cataclysmic fireworks called supernovae. During this explosion their luminosity rivals those of whole galaxies. Supernovae eject most of their mass into space where it forms the basis for the next generation of stars. The stellar centers, however, become enormously compressed and --if the star was not too massive-- the explosion produces a neutron star, or otherwise a black hole of a few solar masses. Neutron stars can be thought of as gigantic atomic nuclei: with a mass of about 1.4 solar masses and radii of only 12 km their densities exceed $10^{14}\ \mathrm{gcm}^{-3}$, the density of an atomic nucleus.
In some cases these exotic stars are observed in binary systems where they orbit their common centre of mass. Due to their enormous compactness such stars can revolve around each other at very small separations and in such systems strong-field gravity effects become important, making such systems excellent laboratories to test theories such as Einstein's theory of General Relativity. In fact, the first indirect evidence for the existence of gravitational waves came exactly from such a system and it earned its discoverers, Russel Hulse and Joseph Taylor, the Nobel Prize for Physics in 1993. One implication of the emission of gravitational waves is that the binary orbit shrinks further until the stars finally merge. This releases gigantic amounts of gravitational energy, more than the Sun could radiate away during the whole lifetime of the Universe. The final merger most likely causes (a

fraction) of the brightest explosions in the Universe since its beginning in the Big Bang, so-called Gamma-Ray Bursts.

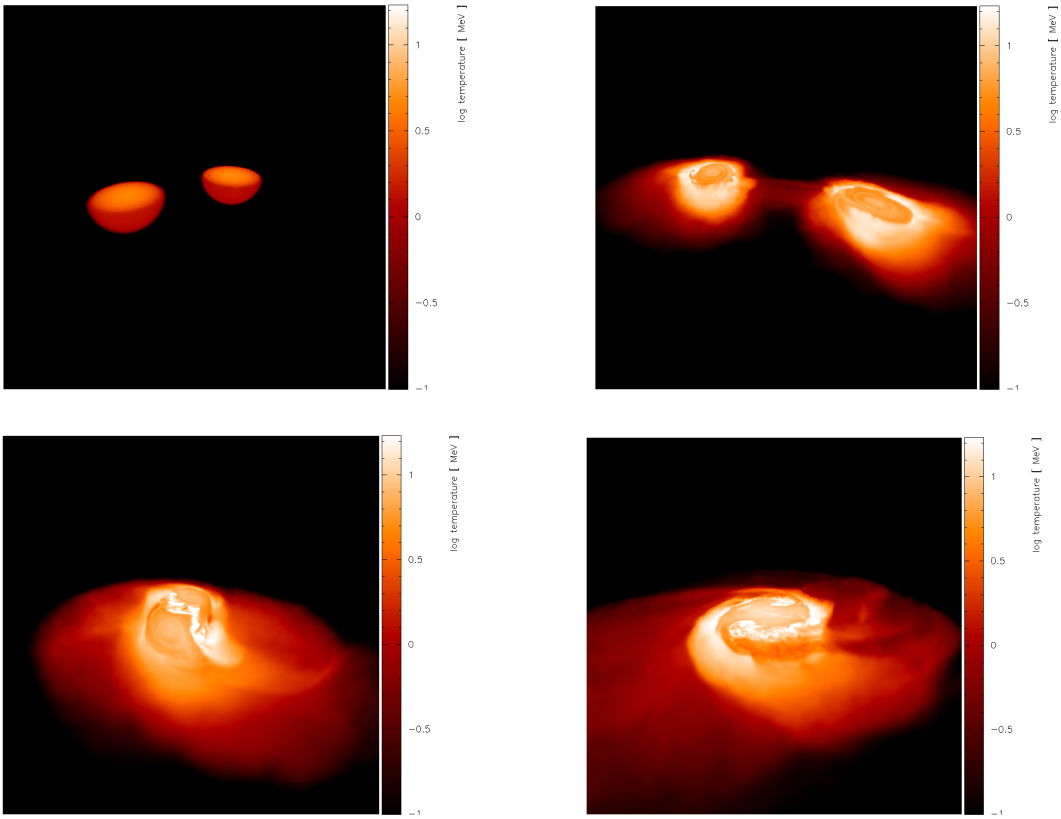

Figure 1. Collision of a 1.3 and a 1.4 $M_{\odot}$ neutron star with an impact strength of $\beta = 2$. Shown are volume renderings of the temperature (at t = 1.49, 3.83, 6.27 and 8.32 ms after simulation start), only matter below the orbital plane is shown.

A variant to this theme are dynamical collisions of compact objects. In the solar neighborhood the density of stars is only moderate, there is about one star in every cube of 3 light years of edge length. There are however, regions in the Universe where this is very different: in the cores of Globular Star Clusters the same volume can contain as many as 100 millions of stars and under these conditions stars frequently suffer direct collisions. If two compact objects collide their overall energetics is similar to merger but their dynamics --and therefore their gravitational wave emission-- is very different. In our HLRN project we study the question how different mergers and collisions are in a) their gravitational wave, b) neutrino and c) electromagnetic emission. Moreover, we want to understand d) what their contribution to the cosmic inventory of heavy nuclei is.

3. Recent Results

We have performed a very large set of simulations where we have explored the parameter space of neutron star mergers with unprecedented breadth. One example of a collision between a 1.3 and 1.4 solar mass neutron star is shown in Fig 1. This simulation was run at very high resolution, it took more than 6 months on 128 processors (the major bottleneck of such a simulations is the enormous sound speed in neutron star matter: it is about 30 % of the speed of light; the sound speed sets via the Courant-Friedrichs-Lewy stability criterion

the allowed numerical time step). Another example, the encounter of a 1.3 solar mass neutron star with a black hole of 5 solar masses, is shown in Fig 2. Interestingly, the core of the neutron star survives several close encounters with the black hole without being disrupted.
The major results that were obtained so far are laid down in four publications [1,2,3,4], several more are currently being prepared for publication. We have calculated how the dynamics of mergers and collisions differ [1]. This has serious consequences for their gravitational wave and neutrino emission and also for their potential to launch a Gamma-Ray Burst. We have put a particular focus on the material that is dynamically ejected in such a compact object encounter. We make predictions for electromagnetic, transient signals that accompany a compact binary merger and collision [1,2]. We have identified two such signals: a) so-called "macronovae" and b) longer lasting radio flares. Macronovae result from the radioactive decays of heavy nuclei within the ejected material. Being powered by radioactivity they are not too different from a supernova explosion, but with their larger velocities and smaller amounts of radioactive material they evolve on much shorter time scales of only about one day. Most interestingly, the resulting nuclei form a pattern that fits the observed distribution of the heaviest elements in the Universe (including gold and platinum; so-called "rapid neutron capture elements") very well [3]. This makes compact binary mergers prime candidates for the cosmic source of these elements. Of order 1 % of the binary mass is dynamically flung into the surrounding galaxy at velocities of 10 % of the speed of light. When this material dissipates its kinetic energy in the surrounding gas it drives strong shocks which in turn produce long-lasting radio flares. These flares reach their peak luminosity a few years after the merger and should be detectable for years [2].

Outlook

We have investigated in detail the fate of two compact objects, either neutron stars or a neutron star with a stellar-mass black hole, that either merge after having having been driven together by the emission of gravitational waves or that collide dynamically, say, in a Globular Star Cluster. We have predicted in detail the observable signatures in various channels: gravitational waves, neutrinos and electromagnetic emission. Such predictions will substantially enhance the effective sensitivity of existing gravitational wave detector facilities such as Geo600, LIGO, VIRGO.
Our future efforts will focus on enhancing and refining further the physics input in our simulations (more General Relativity, more refined nuclear heating physics) and implementing computationally more efficient gravity solvers.

Publications

[1] *The multi-messenger picture of compact object encounters: binary mergers versus dynamical collisions,* S. Rosswog, T. Piran and E. Nakar, Monthly Notices of the Royal Astronomical Society in press, eprint: arXiv:1204.6240
[2] *The electromagnetic signals of neutron star mergers*, T.Piran, E. Nakar and S. Rosswog, Monthly Notices of the Royal Astronomical Society in press, eprint:arXiv:1204.6242
[3] *On the astrophysical robustness of neutron star merger r-process*, O. Korobkin, S. Rosswog, A. Arcones, C. Winteler, Monthly Notices of the Royal Astronomical Society 426, 1940 (2012)
[4] *The dynamic ejecta of compact object mergers and eccentric collisions* Philosophical Transactions A, in press, eprint: arXiv:1210.6549

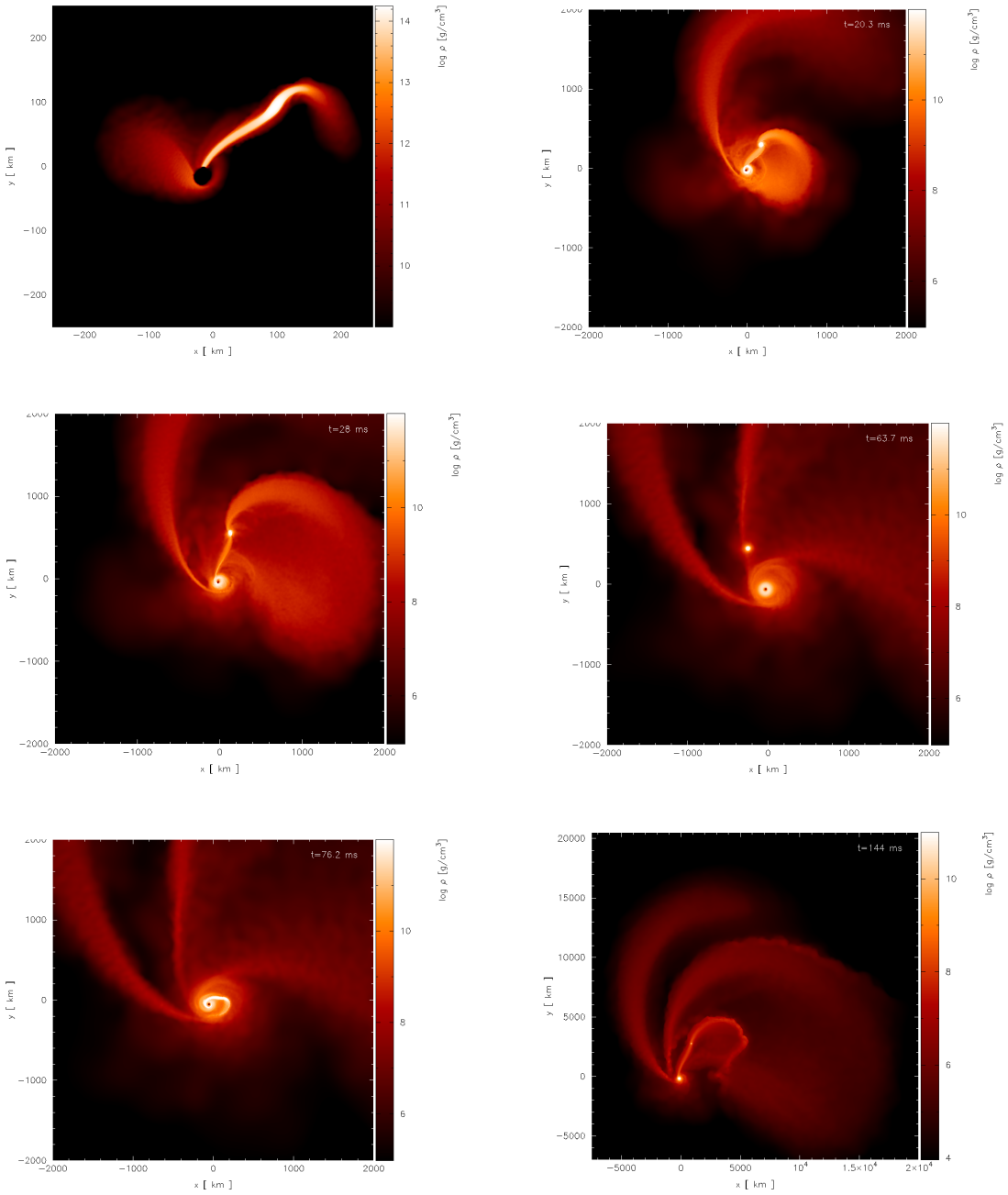

Figure 2. Density cut through orbital plane of run E. Panel one (numbering of the panels is from left to right, from up to down) shows a snapshot just after the first, panel two after the second and panel five just after the third pericenter passage. Each pericenter passage produces a tidal tail. Note that the neutron star core survives even the third pericenter passage. At the end of the simulation it still has a mass of ~ 0.1 $M_{\odot}$ and moves on a close-to-parabolic orbit away from the black hole. Note that the scales are changing between the different snapshots.

6.12 hbp000011: First-principles investigations of hybrid organic-inorganic interfaces

HLRN-Projektkennung:	hbp00011
Laufzeit:	01.10.2012 – 30.09.2013
Projektleiter:	Prof. Dr. Thomas Frauenheim, Dr. Andréia Luisa da Rosa
Projektbearbeiter:	Dr. Andréia Luisa da Rosa, Dr. Michael Lorke, Dr. Liangzhi Kou, Dr. Aline Schoenhalz
Institut / Einrichtung:	Bremen Center for Computational Materials Science, Universität Bremen, Am Fallturm 1, 28359 Bremen

Overview

Understanding the atomistic details and elementary physical and chemical processes of organic molecules on metal oxide surfaces is a topic of pronounced general interest and a necessary prerequisite for applications in several fields, such as optoelectronics, photovoltaics and sensing. Successful surface modification of metal oxides with anchor groups usually requires strong binding. These anchor groups can change the surface wettability, tune their electronic properties and should provide immobilization of further attached biological or organic molecules. Several anchor groups on ZnO surfaces have been suggested, but little is know about their electronic properties and how the conformation of these groups affect the electronic structure of the oxide surface. Furthermore, we would like to understand the atomistic details of optically active dopants in semiconductors, which could be used to make ZnO useful for optoelectronic applications. It is expected that the intra *f*-shell transitions of rare earth these elements are excellent candidates for light emitters.

Current results

In this project we employ density-functional theory and many-body methods to investigate structural, electronic and optical properties of hybrid ZnO/organic interfaces and also rare-earth doped ZnO. First, we have investigated structural, cohesive and electronic properties of ZnO surfaces functionalized with organic molecules using density-functional theory within the generalized-gradient approximation and also using modern hybrid density-functionals. Previously we have identified several groups present in substituted methane molecules CH_3 - X (X= SH, OH, CN, COOH, NH_2 and PO $(OH)_2$) that chemisorb on the non-polar $(10\bar{1}0)$ and $(1\bar{2}10)$ ZnO surfaces. We have analyzed the influence of the surface coverage on the geometries and binding energies under a dry environment. The atomic geometry of one of these functional groups, -COOH, used to modify the ZnO $(10\bar{1}0)$ surfaces is shown in Fig.1.

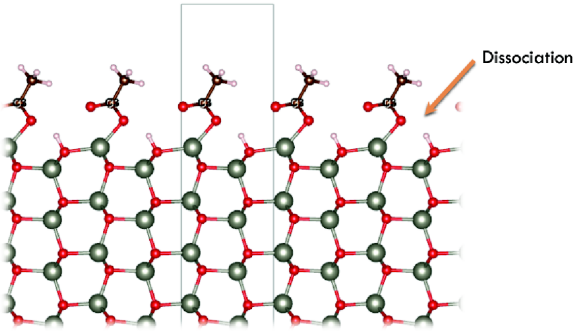

Figure 1: Geometry of the functional group -COOH used to modify the $(10\bar{1}0)$ surfaces using the slab model. A configuration containing a full monolayer coverage is found to be energetically stable.

Although the PBE functional works well for the description of geometry, it does not reproduce the experimental electronic properties of ZnO. The underestimation of band gap in semiconductors within the GGA approximation is a well-known problem. In the case of ZnO this is critical, since the experimental value is 3.3 eV and GGA calculations give a value of 0.7 eV only. Therefore, the use of more accurate and modern density-functionals such as the HSE and PBE0 hybrid functional are needed. We have found two main differences when using hybrid functionals: (i) the opening of the band gap of ZnO, which gives a much better agreement with experimental results and (ii) a better description of the interaction of the organic molecules and the ZnO surface, as can be seen in Fig. 2.

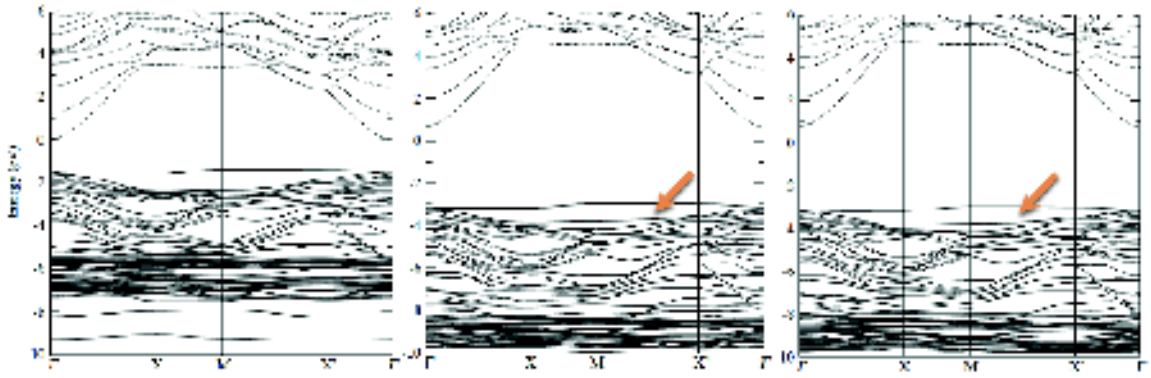

Figure 2: Electronic band structure for CH_3 -COOH on ZnO $(10\bar{1}0)$ surfaces. From left to right, calculations within GGA, PBE0 (not-relaxed) and PBE0 (fully relaxed).

Here we describe the influence of Eu doping on the electronic properties of ZnO and the additional influence of an close-by oxygen vacancy. The latter is of particular importance as oxygen vacancies are common defects in ZnO which can modify the optoelectronic properties of this material significantly. The electronic density of states (DOS) of a single Eu atom in a ZnO matrix is shown for calculations using the PBE0 hybrid functional. The upper panel of Fig. 3 shows the DOS for substitutional Eu on a zinc lattice position. Compared to the bulk material one clearly observed distinct peaks within the band gap that can be attributed to the Eu *p* and *f* electrons. The lower panel shows a very different situation for Eu on zinc lattice position next to an oxygen vacancy. Here the presence of the oxygen vacancy state about 1 eV above the ZnO valence band maximum pushes the Eu *f* states further away. Although there is a large difference in the electronic structure, we conclude that there the presence of Eu alone does not induce transitions in the visibleregion and that other defects should be investigated.

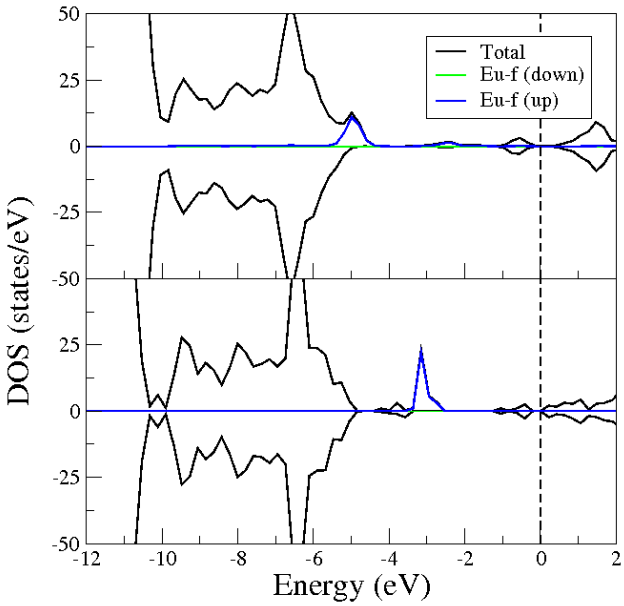

Figure 3: Density of states (DOS) of Eu-doped ZnO. Positive (negative) values correspond to spin up (down). Upper panel: DOS for Eu incorporated substitutionally on a Zn lattice position. Lower panel: DOS for Eu incorporated substitutionally on Zn lattice position next to an oxygen vacancy.

Outlook

We have performed calculations of the electronic properties of organic molecules adsorbed on ZnO surfaces. The use of hybrid functionals is a step forward towards the understanding of these organic-inorganic interfaces, since it leads to a much better description of the electronic states of these complex systems. Our results helped to understand the organic/inorganic interface on an atomistic scale and are the first steps towards more sophisticated calculations aiming the determination of the optical properties of these systems. The next step in the project will be to investigate more complex molecules, such as dyes, which contain the funcional groups identified so far by us. We have also performed calculations for optically active dopants in semiconductors, focusing on Eu doped ZnO. These are important for the carrier transfer into the dopand atoms and therefore directly influence the applicability of the systems in optoelectronic devices. In the future we will investigate the optical properties of these systems using many-body methods, such as GW and Bethe-Salpeter approaches.

Publications

- “Adsorption of monofunctional groups on ZnO surfaces”, N. H. Moreira, A. Dominguez, A. L. Rosa and Th. Frauenheim, PCCP 14, 15445 (2012)
- “Hybrid functionals calculations of ZnO surfaces modified with organic functional groups”, A. Dominguez, N. H. Moreira, A. Schoenhalz, G. Dalpian, A. da Rosa and Th. Fraueheim, to be submitted
- “Rare-earth doped ZnO for solar cell applications”, M. Lorke, A. L. Rosa and Th. Frauenheim, to be submitted

Presentations at conferences

1. CECAM Workshop Modelling realistic inorganic nanostructures: bridging the gap between theory and experiment, Zaragoza, Spanien (2012). “Functionalization of ZnO surfaces with organic molecules: structure and electronic properties” (invited)
2. SBPMat, Florianopolis, Brazil (2012). “Functionalization of ZnO with Organic Molecules from Atomistic Modeling” (invited)
3. CECAM conference Energy from the Sun: Computational Chemists and Physicists Take up the Challenge, Chia Laguna, Italy (2012). “Functionalization of ZnO with Organic Molecules from Atomistic Modeling”
4. Electronic structure theory for materials modeling: from early days to current success, Stockholm, Sweden (2012). “Atomistic simulations of organic/inorganic interfaces”
5. DPG Meeting, Regensburg, Germany (2013). “First-principles calculations of electronic and optical properties of ZnO nanowires”